856

"NEUTRON RADIOGRAPHIC STUDIES"

AT THE CHALK RIVER NUCLEAR REACTOR

by

P.S.W. Chan

"PART A:" INDUSTRIAL PROJECT*

A project report submitted in partial fulfillment of the requirements for the degree of

Master of Engineering

Dept. of Engineering Physics

McMaster University

Hamilton, Ontario

April 1974

*One of two project reports. The other is designated PART B: MCMASTER (ON-CAMPUS) PROJECT.

TITLE (PART A) : Neutron Radiographic Studies At The Chalk River Nuclear Reactor

AUTHOR : P. S. W. Chan

SUPERVISOR : Dr. A. A. Harms

NUMBER OF PAGES : 39

MASTER OF ENGINEERING

(Engineering Physics)

McMASTER UNIVERSITY

Hamilton, Ontario

Index

1. INTRODUCTION

The neutron radiographic facility at the Chalk River NRX reactor is being used for the non-destructive examination of unirradiated and irradiated fuel elements clad with zirconium-based alloys and containing either sintered UO_2 pellets or cast uranium-alloy rods. The author used the facility to perform three main tasks during his 1972 summer internship with Atomic Energy of Canada Limited. Those were to determine the uniformity and cadmium ratio of the neutron beam of the facility, to develop a quantitative method for determining hydrogen concentrations in zirconium-based alloys, and to assess track-etch neutron radiography for examining fuel elements. The following sections describe these tasks in appropriate detail.

2. UNIFORMITY AND CADMIUM RATIO OF THE NEUTRON BEAM

2.1 General

Neutron radiographs with uniform contrast and good image resolution require a well collimated neutron beam of uniform intensity over the object plane. Also, if the neutron beam contains a useful fraction (0.1) of neutrons with energies in the epithermal energy region (0.3 to 10^4 eV), the beam may be particularly useful for radiographing fuel materials which contain plutonium (1). Typical reactor-grade plutonium contains 92 at% of

^{239}Pu and 7 at% ^{240}Pu, and these isotopes exhibit strong neutron absorption resonances in the epithermal region, i.e. at neutron energies of 0.3 eV (5×10^3 barns) and 1.0 eV (10^5 barns), respectively.

The fraction of epithermal neutrons in a given neutron beam is conveniently indicated by its cadmium ratio when measured by beam activation of indium samples which are activated either bare or covered with 0.7 - 0.8 mm. thick cadmium sheet (2). The indium samples are kept very thin (0.1 mg of indium/cm^2 equivalent density) to avoid effects due to self shielding in the sample. The cadmium ratio (CdR) is

$$CdR = \frac{\text{activity induced in bare sample}}{\text{activity induced in covered sample}}$$

Essentially, the covered samples are activated by the epithermal neutrons only. The induced activity is enhanced by using indium which exhibits a strong resonance absorption(3×10^4 barns) at a neutron energy of 1.44 eV. Thus the cadmium ratio obtained indicates more the fraction of indium resonance neutrons in the beam, rather than that of the total number of epithermal neutrons (2). Nevertheless, the ratio is an immediate indication of the epithermal content of the neutron beam and of the beam's usefullness for radiographing plutonium-containing reactor fuels.

2.2 Experimental

Discs of aluminium - 1 wt% indium alloy, 10 mm in diameter and 0.13 mm thick, were used for the beam activations (equivalent indium thickness 0.4 mg/cm^2). Their activation and decay is summarized by the reaction

$$^{115}In + n \rightarrow ^{116}In \quad (54 \text{ min}) \rightarrow ^{116}Sn + (\beta, \gamma),$$

and the activity (C) of an irradiated disc is related directly to the incident neutron flux (ϕ) by (3) :

$$C \approx \phi(\epsilon\Sigma M/\rho\lambda)(1-e^{-\lambda t_1})(e^{-\lambda(t_2-t_1)})(1-e^{-\lambda(t_3-t_2)}) \qquad \ldots(1)$$

where t_1 = time in seconds at removal of disc from neutron beam (disc inserted into beam at zero time),

t_2 = time in seconds at beginning of counting period,

t_3 = time in seconds at end of counting period

λ = decay constant of ^{116}In induced by the irradiation (1.284×10^{-2} min^{-1}),

ρ = indium density in disc in grams of indium/cm^3 of alloy,

M = mass of indium in alloy disc in grams,

Σ = neutron energy-averaged macroscopic neutron cross section section for the $^{115}In \rightarrow ^{116}In$ (54 min) reaction noted above,

ϵ = efficiency of the radiation counter used to measure the disc activity

ϕ = neutron flux in n/cm^2s,

and C_t = total number of counts from the activated disc registered by the counter between t_2 and t_3 seconds.

The activation of the 4.23% abundant ^{113}In isotope in natural indium was ignored, since its contribution to the number of counts registered can be shown to be negligible with the values of t_1 and t_3 used, typically 4×10^3 and 1×10^2 seconds, respectively.

The activities of the irradiated discs were measured using an automated counter equipped with NaI detectors which were sensitive primarily to gamma radiation. Relative neutron intensities and cadmium ratios were determined in 24 positions in a 130 mm x 180 mm area of the object plane in the radiographic facility. The neutron intensity had a maximum variation of approximately 5% across the area. The average cadmium ratio was 34.7 with maximum variations of 1.5.

2.3 Conclusion

The satisfactory uniformity of neutron intensity across the object plane ensures that high quality neutron radiographs can be obtained. However, the cadmium ratio obtained indicates that the fraction of epithermal neutrons available in the neutron beam is very small, and that attempts to employ resonance neutron absorption for examining plutonium-containing reactor fuels would be unattractive with the present neutron beam exposure times of about 1 hour.

3. MEASUREMENT OF HYDROGEN CONCENTRATIONS IN ZIRCONIUM ALLOYS

3.1 General

Neutron radiography is a powerful technique for detecting hydrogen in zirconium-based alloys because of the large thermal neutron scattering cross section of hydrogen (35 barns) compared to that of zirconium (6 barns). Hydrided zircaloy components will attenuate thermal neutrons more strongly than non-hydrided ones. Thus in the radiographic arrangement; the transmitted neutron beam through the hydrided component will be less intense than that through the non-hydrided counterpart. The difference in neutron intensity is recorded on photographic film as a difference in image opaqueness which, in turn, can be measured by a scanning microdensitometer and related quantitatively to the amount of hydrogen in the hydrided component.

The following sections are concerned with the development, testing and application of the relation between the hydrogen concentrations in a hydrided Zircaloy component and the diffuse optical densities of its radiographic image. (Because the thermal neutron scattering cross section of deuterium (7 barns) is comparable to that of zirconium, the radiographic technique would not be useful for measuring the degree of deuterium pick-up by zirconium alloy components, e.g. by fuel element sheathing exposed to the D_2O coolant in the Canadian power reactors.)

3.2 Neutron Attenuation by the Object

For any small area of an abject, the attenuation of the incident neutron beam of intensity $\phi_o (n/cm^2 s)$ depends on the object's thickness measured in a direction parallel to the beam $x_i (cm)$ and macroscopic cross section $\Sigma_i (cm^{-1})$. The intensity of the neutron beam transmitted through the object ϕ_i is given approximately by

$$\phi_i = \phi_o \, e^{-\Sigma_i x_i} \qquad \ldots(1)$$

3.3 Activation of the Neutron-Imaging Foil

In the radiographic arrangement used, a well collimated, slightly divergent beam of thermal neutrons impinges on the object being radiographed. A thin foil of natural dysprosium is positioned immediately behind the object in a plane perpendicular to the beam axis. The foil becomes activated according to the intensity of the attenuated neutron beam passing through the object, and to the intensity of the non-attenuated beam passing around the object. (The levels of activity reached in the "neutron-imaging" foil depend on the time in the neutron beam, but this is usually chosen so that sufficient foil activity is developed that it can be conveniently recorded subsequently on photographic film). The transfer of the " radiographic image " in the foil to the photo film is carried out in a suitable darkroom by pressure-contact

between the foil and the film emulsion. The principal cause of latent-image formation in the film emulsion are the β-particles emitted from the (β,γ)-active foil (4).

The neutron-beam activation of the dysprosium foil and the subsequent β-particle exposure to the photo film follow the standard equations describing the growth and decay of a radioactive species. Specifically, the β-particle exposure to a given small area of the photo film can be shown, by rearranging Equation 1 of Section 2.2 above, to be E_i where :

$$E_i = k\phi_i \, (1-e^{-\lambda t_1})(e^{-\lambda (t_2-t_1)})(1-e^{-\lambda (t_3-t_2)}) \qquad \ldots(3)$$

where

ϕ_i = intensity of neutron beam incident on the small area of dysprosium imaging foil which is in contact with the given small area of photo film, n/cm^2s,

t_1 = time in seconds at removal of imaging foil from the neutron beam (foil inserted into beam at zero time).

t_2 = time in seconds at beginning of contact time between activated foil and photo film.

t_3 = time in seconds at end of foil/film contact.

k_1 = a constant for a given dysprosium foil of uniform thickness and density

The values of t_1 , t_2 , and t_3 are common throughout the complete area of photo film making up a given neutron radiograph. Consequently, the β-particle exposure to a particular area of the film depends only on the intensity of the neutron beam at

the corresponding area on the dysprosium imaging foil. (For purposes of simplicity, it was assumed that the neutron beam incident on the sample was of constant intensity throughout the beam exposure time t_1.) Consequently, we may write

$$E_i = k_2 \phi_i \qquad \ldots\ldots (4)$$

where k_2 = a constant

3.4 Response of the Photographic Film to β-Particle Exposure

The neutron radiographs in this work were obtained on Kodak, single emulsion type SR-54 film. The 0.31-1.31 MeV β-particles from the decay of the ^{165}Dy isotope produced in the dysprosium imaging foils have sufficient energy to pass completely through the film emulsion and substrate. Consequently, it was assumed that their effectiveness in latent image development was closely similar to that of X-rays.

The characteristic curve showing the developed film density versus X-ray exposure for the SR-54 film was available from the manufacturers (5) and is given in Figure 1, curve A. Most modern X-ray films exhibit a near-linear dependence of film density on exposure (6); curve B in Figure 1 was derived from curve A, and shows that type SR-54 film follows this behaviour. Thus in the present analysis, the relation

The relations are best developed by first referring to Figure 2 which shows three Zircaloy slab samples arranged for neutron radiography. The central sample is a "control" of thickness x_1 cm containing a negligible concentration of hydrogen. The slab of thickness x_2 contains an unknown concentration of hydrogen, and the slab of thickness x_3 contains a known concentration of hydrogen. The incident neutron flux is ϕ_o n/cm^{2}s and is assumed uniform across the slabs.

Figure 3 shows, schematically, the trace obtained from a recording densitometer after scanning across the radiographic image of the three slabs. The electrical circuitry of the densitometer results in the vertical distances d_o, d_1, d_2 and d_3 being directly proportional to the film densities of, respectively, the "background", the control sample, the sample of unknown hydrogen content and the sample of known hydrogen content. Frequently, the densitometer is used to record only the upper part of Figure 3 i.e. that above the dashed line, since then the height differences (d_o-d_1), (d_o-d_2) and (d_o-d_3) can be recorded and measured more accurately.

Using equation 6 we can write

$$d_o = k_6\phi_o \qquad \ldots(7)$$

$$d_1 = k_6\phi_o e^{-\Sigma_1 x_1} \qquad \ldots(8)$$

$$d_2 = k_6\phi_o e^{-(\Sigma_1+\Sigma_2)x_2} \qquad \ldots(9)$$

$$\text{and } d_3 = k_6 \phi_o e^{-(\Sigma_1+\Sigma_3)x_3} \quad \ldots\ldots\ldots (10)$$

where Σ_1 = the macroscopic cross section for thermal neutrons of Zircaloy in cm^{-1}.

Σ_2 and Σ_3 = respectively, the effective macroscopic cross section of the hydrogen contained by the samples of unknown and known hydrogen content in cm^{-1}.

and k_6 is a constant.

Equations 7 to 10 can be used to express

(i) the known hydrogen content of the standard hydrided sample in terms of the height differences (d_o-d_1) and (d_o-d_3) and the sample thickness x_1 and x_3. Thus, denoting (d_o-d_1) by Δd_1, we can write from equations 7,8 and 10,

$$\Delta d_3/\Delta d_1 = (1-e^{-(\Sigma_1+\Sigma_3)x_3})/(1-e^{-\Sigma_1 x_1}) \quad \ldots(11)$$

which can be reduced to the approximate form

$$\Delta d_3/\Delta d_1 \approx (\Sigma_1+\Sigma_3)x_3/\Sigma_1 x_1 \quad \ldots(12)$$

Since Σ_3 can be assumed to be directly proportional to the concentration of hydrogen in the standard hydrided sample, H_3 say, equation 12 can be written

$$\underline{H_3 \approx k_7 \left\{(\Delta d_3/\Delta d_1((x_1/x_3)-1\right\}} \quad \ldots(13)$$

where k_7 is a constant.

(ii) the hydrogen concentration in the slab of unknown hydrogen content in terms of the height differences Δd_1, sample thicknesses

x_i and the known hydrogen concentration in the standard hydrided sample H_3, thus -

combining equations 7,8 and 9,

$$\Delta d_2/\Delta d_1 = (1-e^{-(\Sigma_1+\Sigma_2)x_2})/(1-e^{-\Sigma_1 x_1}) \qquad \ldots(14)$$

which, like equation 11, can be reduced to the approximate form

$$\Delta d_2/\Delta d_1 \approx (\Sigma_1+\Sigma_2)x_2/\Sigma_1 x_1 \qquad \ldots(15)$$

Since Σ_2 can be assumed to be directly proportioned to the concentration of hydrogen in the sample of unknown hydrogen content, H_2 say, equation 15 can be written

$$H_2 \approx k_7 \left\{(\Delta d_2/\Delta d_1)(x_1/x_2)-1\right\} \qquad \ldots(16)$$

where k_7 is the same proportional constant used in equation 13. By combining equations 13 and 16 we obtain

$$H_2 \approx H_3(x_3/x_2)(x_1\Delta d_2-x_2\Delta d_1)/(x_1\Delta d_3-x_3\Delta d_1) \qquad \ldots(17)$$

As a final note to this section, the effect of reducing equations 11 and 14 above to their approximate forms was checked as follows.

For thermal neutrons, $\Sigma = 0.26\ cm^{-1}$ for pure zirconium and $(\Sigma+\Sigma_H) \approx 1.8\ cm^{-1}$ for pure ZrH_2 (7), where Σ_H is the effective thermal neutron macroscopic cross section for the hydrogen concentration in ZrH_2. Thus Σ_H itself is roughly $1.5\ cm^{-1}$, and corresponds to a hydrogen concentration of 2×10^4 parts of hydrogen per million parts of zirconium by weight (ppm). It

was known that for the present work, the hydrogen content of samples would not exceed about 10^3 ppm. For this concentration, Σ_H would assume a value of 0.08 cm^{-1}. Using this value in equation 12 and putting $x_1 = x_3 = 1$ cm, gives a value for $\Delta d_3/\Delta d_1$ which is some 2.5% larger than that calculated from the more exact equation 11. This error was not considered a serious limitation in the present work as most of the hydrided samples used contained less than 10^3 ppm hydrogen.

3.7 Experimental Verification of Equation 13

For verification of this equation, five 6.73 mm-thick and five 8.38 mm-thick sections of Zircaloy tubing were uniformly hydrided to selected levels between 100 and 1200 ppm of hydrogen. These will be referred to as "standards". Short sections of non-hydrided Zircaloy tubing having the same thicknesses were used as " control " sections.

Figure 4 is a positive print from a thermal neutron radiograph of the standard hydrided sections with the controls positioned in between. Each section was wired in place to minimize movement during exposure to the neutron beam. Apparently, the strong gamma component of the neutron beam ($\sim$ 600 R/h) sometimes caused flexing of the samples, presumably due to differential thermal expansions induced by gamma heating.

Densitometer scans were made on the original neutron

radiograph along the lines AA and BB in Figure 4. Part of the resulting densitometer trace is reproduced in Figure 5. Because of the arrangement of the sheath sections, 2 values of the height difference Δd_3 could be obtained from one scan for each hydrided standard, i.e $(\Delta d_3)_1$ and $(\Delta d_3)_2$ in Figure 5. Correspondingly, two values of the height difference Δd_1 were obtained from the control sections positioned either side of the hydrided standards, i.e. $(\Delta d_1)_1$ and $(\Delta d_1)_2$ in Figure 5.

Table 1 gives the measured height differences appropriate to each hydrided standard, and the average value of the ratios $(\Delta d_3)_1/(\Delta d_1)_1$ and $(\Delta d_3)_2/(\Delta d_1)_2$ for each standard. The averages are plotted against the hydrogen concentration in each standard in Figure 6. The variation of the ratio $\Delta d_3/\Delta d_1$ with hydrogen concentration followed equation 13 satisfactorily up to about 1000 ppm of hydrogen. Above this concentration, the two ratios obtained showed the expected divergence resulting from the approximate nature of equation 13. Nevertheless, for hydrogen concentrations up to 1000 ppm, the results indicated that concentrations down to 100 ppm would be detectable. However, the ratio $\Delta d_3/\Delta d_1$ could be measured from the densitometer traces to a precision of about ±5%. Figure 6 indicates that this corresponds to a precision in measuring hydrogen concentration of about ±100 ppm.

3.8 Use of Equation 17 to Determine Unknown Hydrogen Concentrations in a Zircaloy Component

A Zircaloy pressure tube from the X-7 test loop of the Chalk River NRX Reactor was removed after a 6-year service period, during which organic coolant (a mixture of hydrogenated terphenyls) had flowed through the vertically-positioned tube at temperatures near 300°C. It was expected that the ends of the tube would be hydrided because of temperature gradients along the rolled-joint used to join the tube to the external steel piping of the loop.

The upper end of the tube was available for examination, and Figure 7 shows how it was cut into samples for radiography. These were 2 longitudinal, diametrally opposed strips ($3\frac{1}{2}$ " long x 3/8 " wide) A1 and B1, and 16 "half-sections" (3/8 " wide) A2 to A9 and B2 to B9, see Figure 7. Appropriate "controls" were cut from an archive sample of the pressure tube. Their dimensions were made as close as possible to those of the half-sections and strips from the hydrided tube.

For radiography, the half-sections and strips were wired in position onto an aluminum plate with the controls between them. A hydrided Zircaloy sheath section (1150 ppm H_2) was used as a standard, and a similar section of non-hydrided Zircaloy sheath was used as an appropriate "control" for the standard.

Figures 8 and 9 are positive prints from the neutron radiographs of the pressure-tube samples and their controls. The dark oblongs are brass blocks which kept the samples at a uniform distance from the dysprosium imaging foils.

The densitometer scans were made along the line DD in Figures 8 and 9, and across the strips A1 and B1 in 16 different locations. The appropriate height-difference ratios were obtained from the densitometer traces, and equation 17 was used to calculate hydrogen concentrations.

Figure 10 gives results obtained for the half-sections, and Figure 11 gives those for the strips. Necessarily, each value of hydrogen concentration is an average one over the thickness of each section or strip.

Generally, the results in Figures 10 and 11 agreed and indicated hydrogen concentrations $\gtrsim$ 450 ppm near the uppermost end of the pressure tube and $\lesssim$ 200 ppm near the location just below the outer rolled joint ring. A local increase in hydrogen concentration to about 400 ppm was apparent 1.5 inches below the top end, and roughly coincident with one of two circumferential ridges formed in the tube by compression in the rolled-joint.

After the radiographic measurements, the strips A1 and B1 were each cut into 14 pieces, and individual pieces were chemically

analyzed for their hydrogen content. The results agreed closely with those obtained radiographically, and showed that the precision of the radiographic measurements of hydrogen concentration was about ±50 ppm of hydrogen.

Both the observed decrease in hydrogen content starting from the top end of the tube and the amount of hydrogen present were expected from experience with previous reactor pressure tubes that had been exposed to organic coolant, but the local increase to 400 ppm was unexpected. There are several routes for the flow of hydrogen into the pressure tube, and selection of one of these may explain the effect.

3.9 Conclusions

A procedure for determining hydrogen concentrations in zirconium-based alloys from thermal neutron radiographs of these alloys has been developed and successsfully tested. The sensitivity of the method is approximately $\lesssim$ ±100 ppm of hydrogen for samples containing up to about 10^3 ppm of hydrogen. In one application, a sensitivity near ±50 ppm was demonstrated.

4. TRACK ETCH NEUTRON RADIOGRAPHY

4.1 Introduction

In track-etch neutron radiography, plastic films such as cellulose nitrate are placed in close contact with a converter

screen containing boron-10 or lithium-6 isotopes. Heavily charged alpha particles are emitted by the interaction of these isotopes with incident thermal neutrons according to (8)

$$^{10}_{5}B + n \rightarrow ^{4}_{2}He\,(1.4\ MeV) + ^{7}_{3}Li$$

$$^{6}_{3}Li + n \rightarrow ^{4}_{2}He\,(4.7\ MeV) + ^{3}_{1}H$$

The first reaction is preferred in track-etch radiography because of the considerably higher thermal neutron cross-section of boron-10 (3500 barns) compared to lithium-6 (960 barns), and also because of the less energetic alphas produced. The alpha particles leave tracks in the plastics which can be made visible by selectively etching the areas damaged by the alpha-radiation.

The features of the track-etch technique are that

(a) the plastic detectors are insitive to light, eliminating the darkroom operation,

(b) the short range of the alpha particles, typically 15 to 20 microns, gives final images of excellent resolution, and

(c) the plastic detectors are insitive to gamma and β-particle radiations, and therefore can be used for inspecting radioactive samples such as irradiated fuel elements, and for use with neutron beams containing a strong gamma component.

These are some of the advantages over the transfer method, for which a darkroom operation is necessary, and over the direct

method which is not suitable for strongly radioactive objects or when the neutron beam contains a strong gamma component.

4.2 Experimental

Track-etch neutron radiographs were obtained using different combinations of cellulose nitrate films and converter screens containing boron-10. The most promising results were obtained using Kodak-Pathé LR-115 film (9) and a borided steel plate (10).

The LR-115 film is a thin layer ($\lesssim$ 8 micron) of cellulose nitrate on a thicker polyester base. The cellulose nitrate layer is coloured pink to raise the contrast of the image when viewed with transmitted light. Excellent image resolution and good contrast were demonstrated by projecting these track etch radiographs on to a screen with a magnification of approximately 40 times. Comparisons of densitometer traces across the image of a cadmium knife edge in a track-etch radiograph with that in a transfer-exposure radiograph (dysprosium foil and Kodak single-emulsion type-SR 54 film) indicated that the resolution of the track-etch image was at least twice as good as the transfer-exposure image. However, the track-etch contrast was only one-fifth that of the latter.

Figure 12 shows a diagram of a visual image quality indicator (VISQUI) developed at the Argonne National Laboratories (11). This object consists of pieces of cadmium with tiny holes at various separations, sets of cadmium and plastic wires of different dimensions to test resolution, and rows of squares of different neutron absorbers (Cd,In, etc.) of different thicknesses to test image contrast. The arrangement of objects is repeated at three different distances from the base of the VISQUI, resulting in three different separations between each set of objects and the neutron imaging foil during radiography. Visual examination of the radiographic image of the VISQUI quickly indicates the degree of resolution and contrast obtained.

Figure 13 shows thermal neutron radiographs of the VISQUI using the track-etch and transfer-exposure methods. The track-etch radiograph was obtained using the borided plate/LR-115 film combination at an integrated neutron exposure of 3.6×10^{10} n/cm^2, followed by etching in Eastman Kodak VX 007 solution for 15 minutes at 60°C. The transfer-exposure radiograph was obtained using dysprosium foil and Kodak single-emulsion type SR-54 film; the neutron exposure was 7.2×10^{10} n/cm^2, followed by a one hour foil/film contact in a darkroom.

Visually, the contrast in the track-etch radiograph in Figure 13 appeared comparable to that in the transfer-exposure radiograph. However, as noted above, densitometric measurements showed a ratio of about 1:5 in these contrasts in favour of the latter. The superior resolution of the track-etch radiograph is probably not evident in Figure 13. This was probably due to the greater difficulty of reproducing the lower-contrast track-etch radiograph as a positive print compared to that for the transfer-exposure radiograph.

Figure 14 shows positive prints from track-etch and transfer-exposure radiographs of cast-metal reactor fuel rods. The respective neutron exposures and plastic and film processing conditions were identical to those used for the radiographs shown in Figure 13. Comparing the two types of radiograph in Figure 14 shows that the transfer-exposure radiograph contains more information. For example, although both radiograph resolve the axial hole along the hollow metal fuel rod and the interfaces between the solid fuel pieces, the track-etch radiographs fails to show clearly the casting pores in the fuel rods, i.e. the white spots in Figure 14 (b), and the metal-sheath enclosing the rods.

A large number of track-etch radiographs were prepared in an effort to increase the information obtainable from them.

Neutron exposures were varied from 6×10^9 to 7.2×10^{10} n/cm^2, corresponding to from 5 to 60 minutes neutron-beam exposures in the NRX reactor radiographic facility with the reactor at full power (31 MW). Etching times for the exposed LR-115 films were varied between 5 and 35 minutes at 60°C . Radiographs providing the most information were obtained with the highest neutron exposures and longest etching times. These conditions gave pale pink radiographs in which contrast had been reversed (9).

4.3 Conclusion

Track-etch neutron radiographs have been obtained using a borided steel plate combined with Kodak-Pathé LR-115 cellulose nitrate film and Eastmam-Kodak VX 007 etching solution. Satisfactory radiographic resolution and contrast were obtained over a wide range of neutron exposures and etching times. However, the track-etch radiographs were less satisfactory than transfer-exposure radiographs using dysprosium imaging foils with respect to inspecting certain features in nuclear fuel elements.

ACKNOWLEDGEMENTS

For this work, the author was trained to use the radiographic facility by L.C. Berthiaume, who also provided constant assistance in obtaining and interpreting radiographs. Invaluable assistance was also provided by the NRX Reactor Operations staff and by the Reactor Physics Branch.

The author is most grateful to his immediate supervisor A.M. Ross for his stimulating interest in and discussions of the many aspects of the work done during the summer, and to J.R. MacEwan, Branch Head Fuel Materials Branch who also provided guidance in the preparation of this report.

REFERENCES

1. H. Berger, An. Rev. Nucl. Sci., 21, 335 (1971)

2. D. J. Huges, " Pile Neutron Research ", Addison-Wesley Publishing Co. Inc., 1953.

3. W.J. Garland, " Analysis of Neutron Flux Variation in a Pool Type Reactor", Undergraduate Project, McMaster University, 1970

4. R.H. Herz," The Photographic Action of Ionizing Radiations in Dosimetry and Medical, Industrial, Neutron, Auto-and Microradiography ", Wiley-Interscience, New York, p.208 (1969).

5. From Figure 4, "Radiography in Modern Industry", supplement to "Kodak Films for Industrial Radiography", Eastman Kodak Company, Rochester, N.Y, USA (1970).

6. E.g. Ref. 4 p.104.

7. Reactor Handbook, Vol. 1 Materials, 2nd Ed., C.R. Tipton Jr. Ed., Interscience Publishers Inc., New York, P.836-7

8. H.A. Bethe, Rev. Mod. Phys. 22, 213 (1950)

9. J. Barbier, J. Photographic Sci., 19, 108 (1971).

10. Sample from Universal Metalliding, Reston Virginia, U.S.A. The boriding process is described by N.C. Cook, Scientific American,221, (2) 38 (1969).

11. J.P. Barton, J. of Materials, 7, (1) 18, (1972).

TABLE 1

DENSITOMETRIC DATA FOR THE HYDRIDED STANDARD SHEATH SECTIONS

Standard Sheath Section No.	Height Differences		Average of the Ratio $\Delta d_3/\Delta d_1$	Hydrogen Concentration in Standard, ppmH_2
	Δd_3 (Standard) mm	Δd_1 (Control) mm		
1	37.0 36.5	34.5 34.5	1.065	99
2	41.0 41.5	35.0 35.0	1.18	336
3	43.0 42.0	35.0 34.0	1.23	500
4	53.5 54.0	36.0 37.0	1.47	972
5	48.5 50.5	32.5 33.0	1.51	1149
6	30.0 28.5	28.5 26.5	1.06	118
7	33.0 34.5	29.0 29.0	1.16	336
8	36.0 37.0	29.0 29.0	1.26	521
9	39.0 39.0	28.5 28.0	1.38	704
10	41.5 41.0	27.0 27.0	1.53	1175

Sections 1 - 5 thickness 8.38 mm; sections 6 - 10 thickness 6.73mm

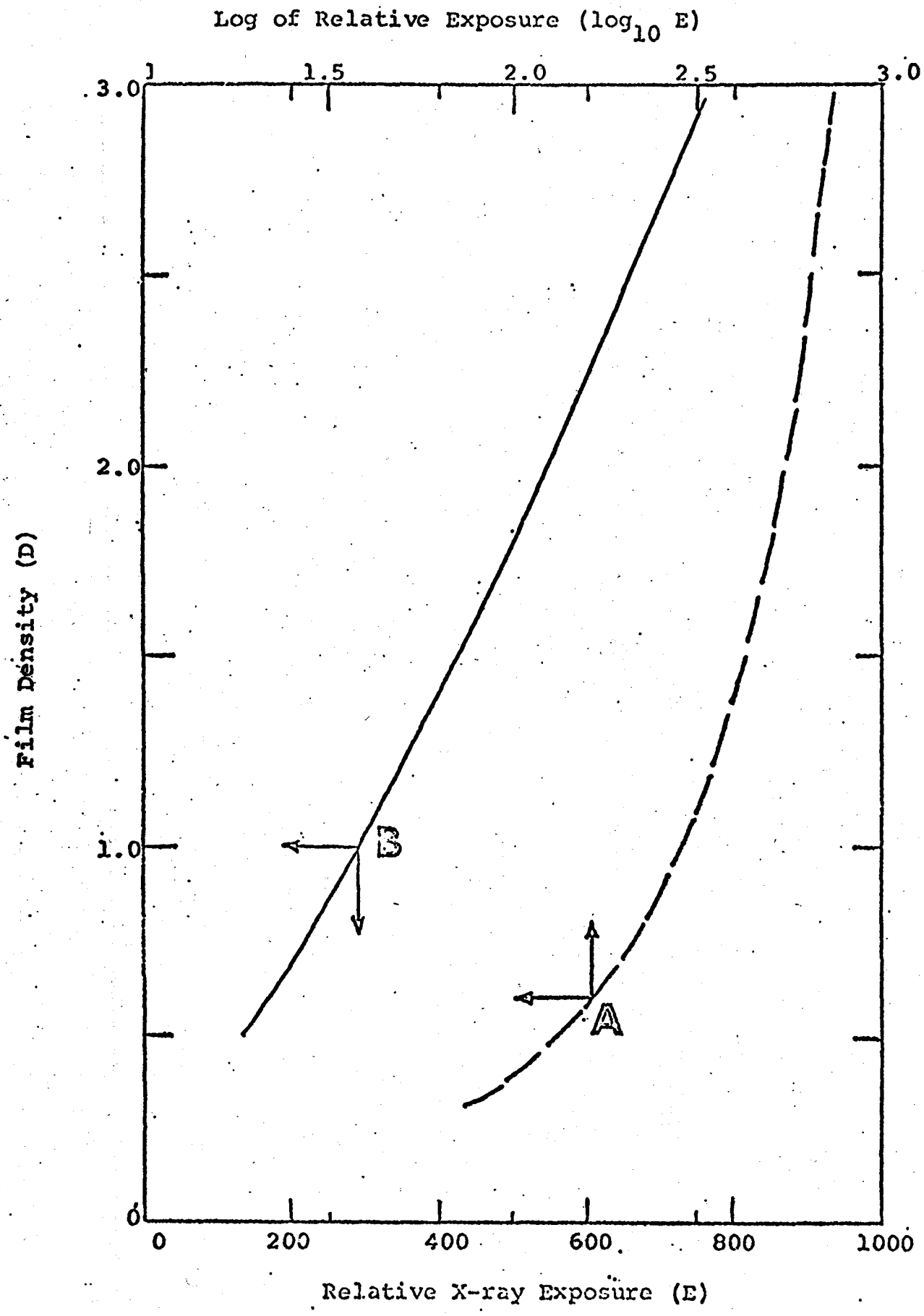

Figure 1 . Density-exposure characteristics for Kodak single-emulsion type SR-54 film.

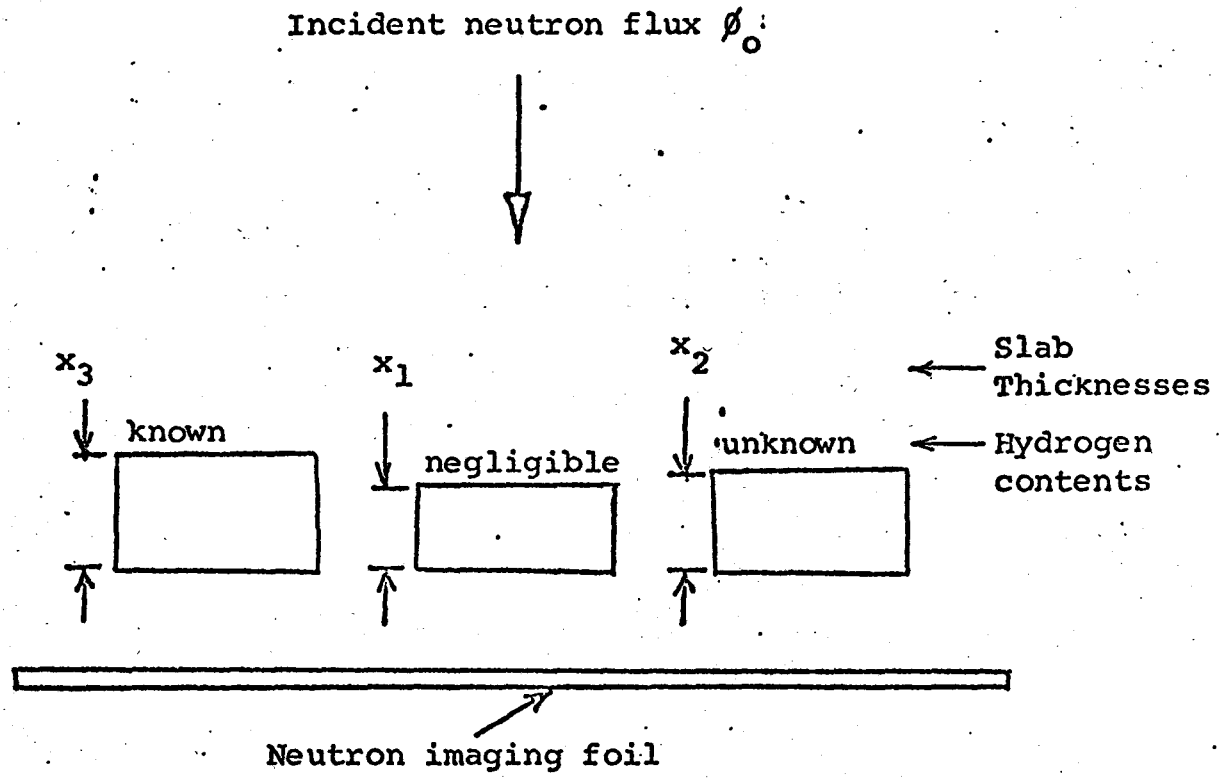

Figure 2 Arrangement of hydrided and non-hydrided slabs for radiography

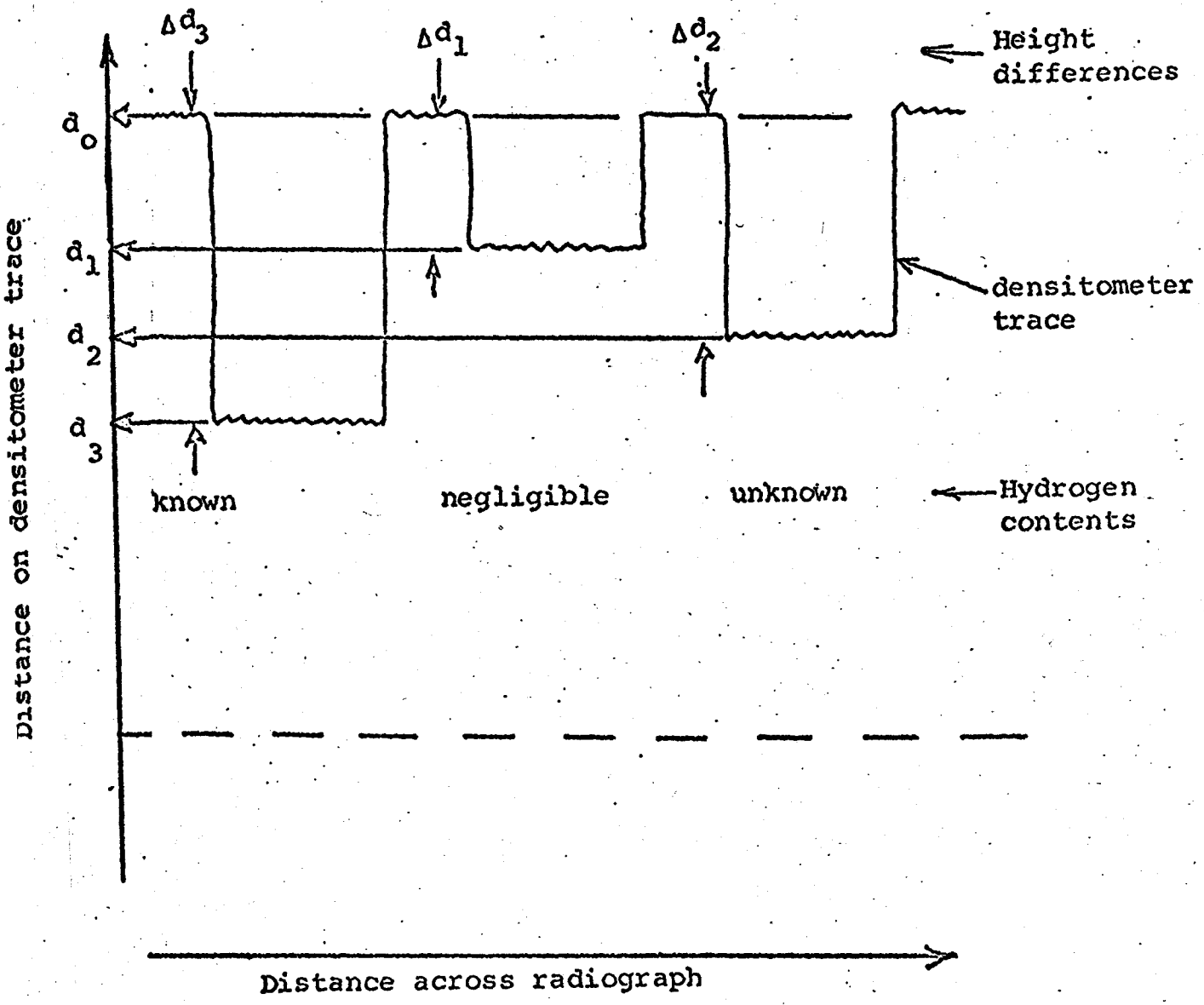

Figure 3 Output of recording densitometer scanning across the radiographic images of the slabs shown in Fig. 2, (schematic).

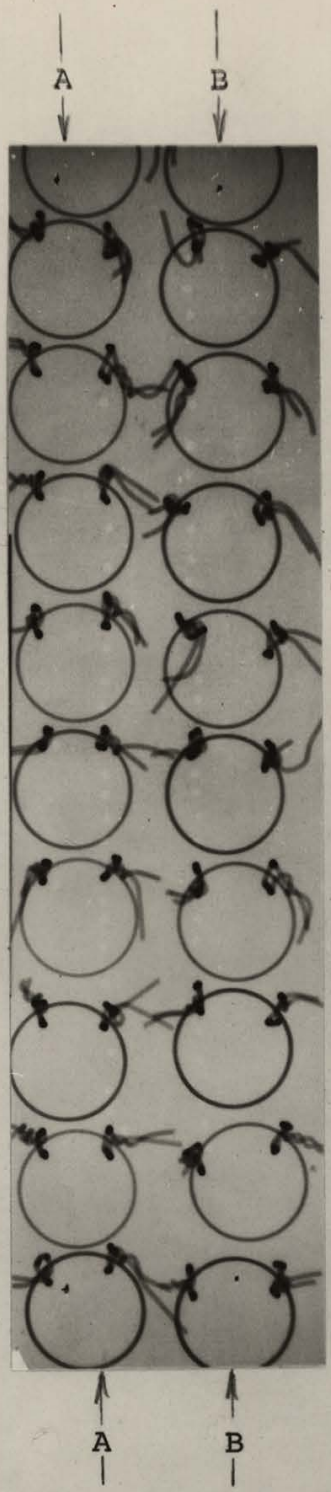

6.73 mm thick Sections	8.38 mm thick Sections
Control	Control
Section No. 6 118 ppm H_2	Section No. 1 199 ppm H_2
Control	Control
Section No. 7 336 ppm H_2	Section No. 2 336 ppm H_2
Control	Control
Section No. 8 521 ppm	Section No. 3 500 ppm H_2
Control	Control
Section No. 9 704 ppm	Section No. 4 972 ppm H_2
Control	Control
Section No. 10 1175 ppm	Section No. 5 1149 ppm H_2

Figure 4 Positive print from neutron radiograph (negative) of hydrided standard sheath sections and non-hydrided control sheath sections. Hydrogen concentrations in each standard (obtained by chemical analysis) are indicated.

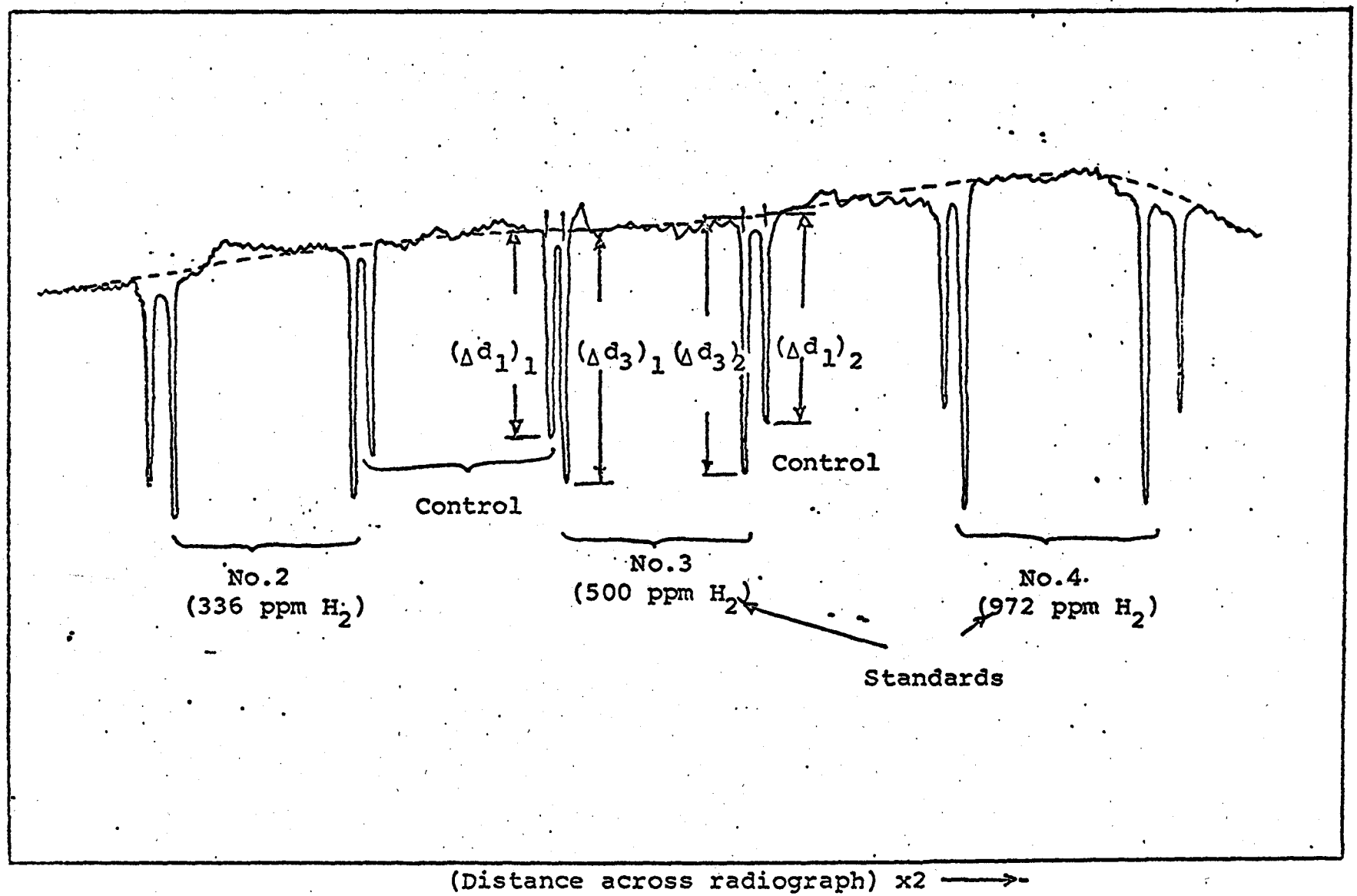

Figure 5 Part of densitometer output after scanning across the radiographic images of the hydrided standard and non-hydrided control sheath sections in Figure.4

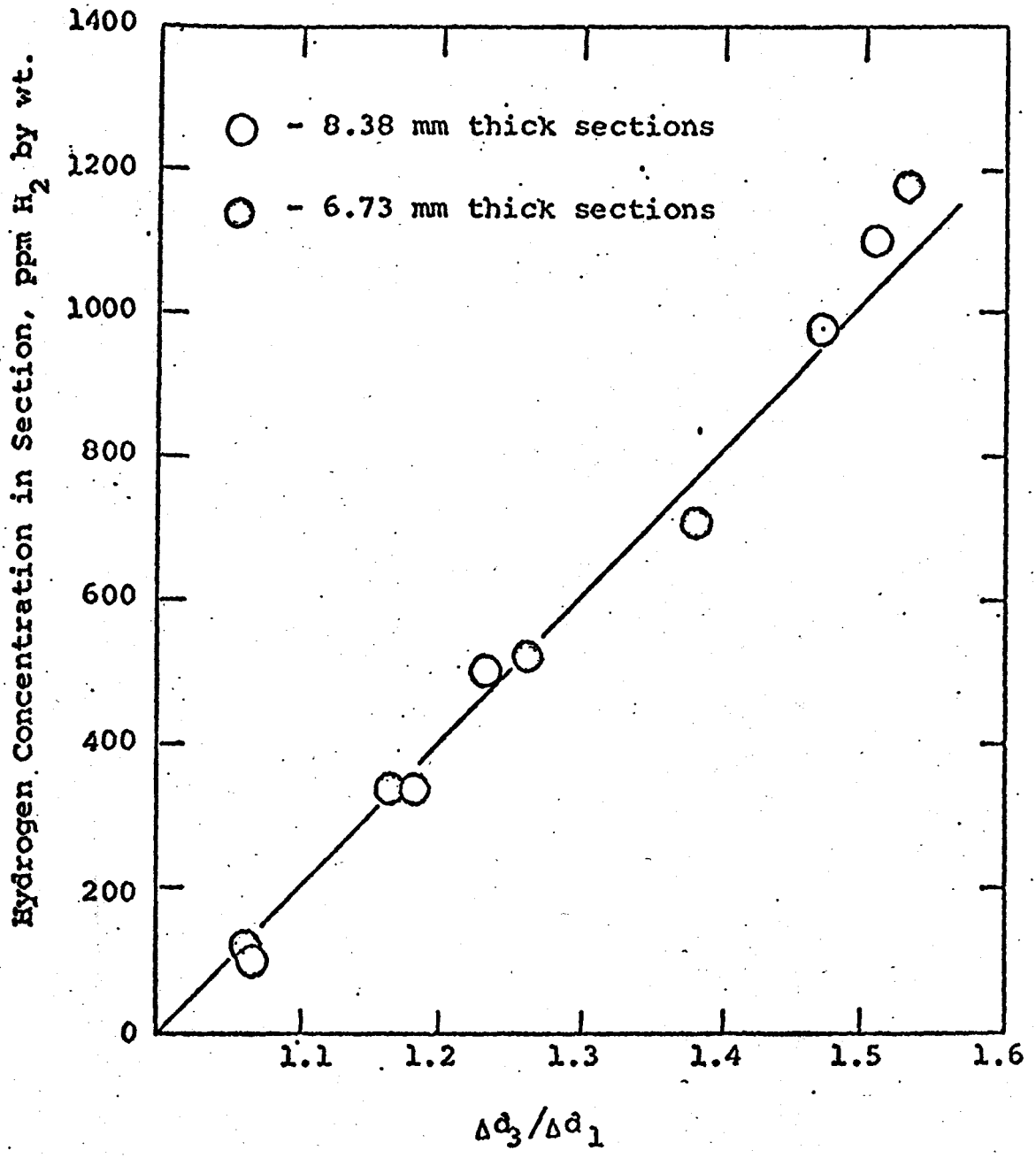

Figure 6 Hydrogen concentration vs the ratio $\Delta d_3/\Delta d_1$ for 10 standard hydrided Zircaloy sheath sections

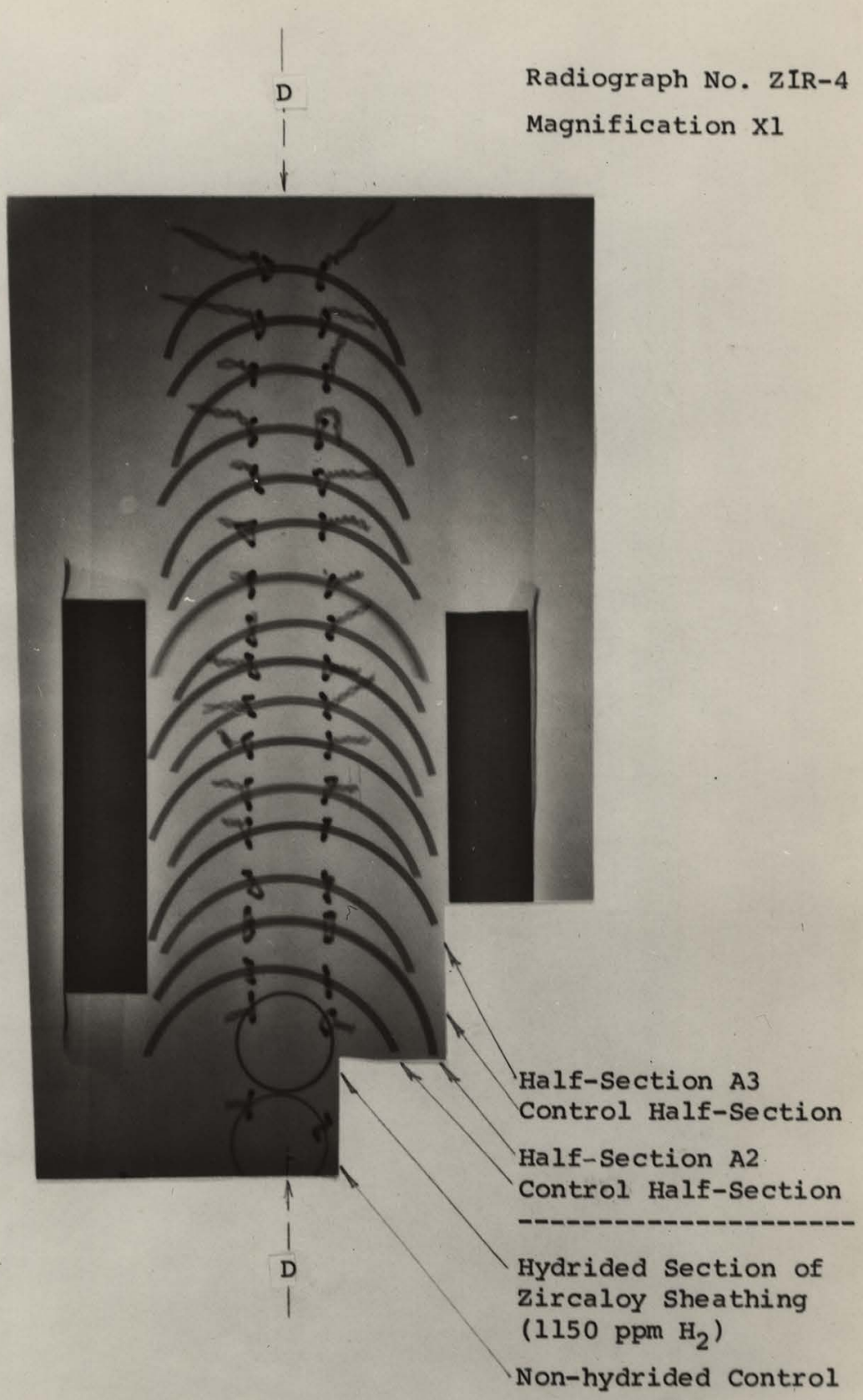

Figure 8 Positive Print from the Neutron Radiograph of the A-series of half-sections

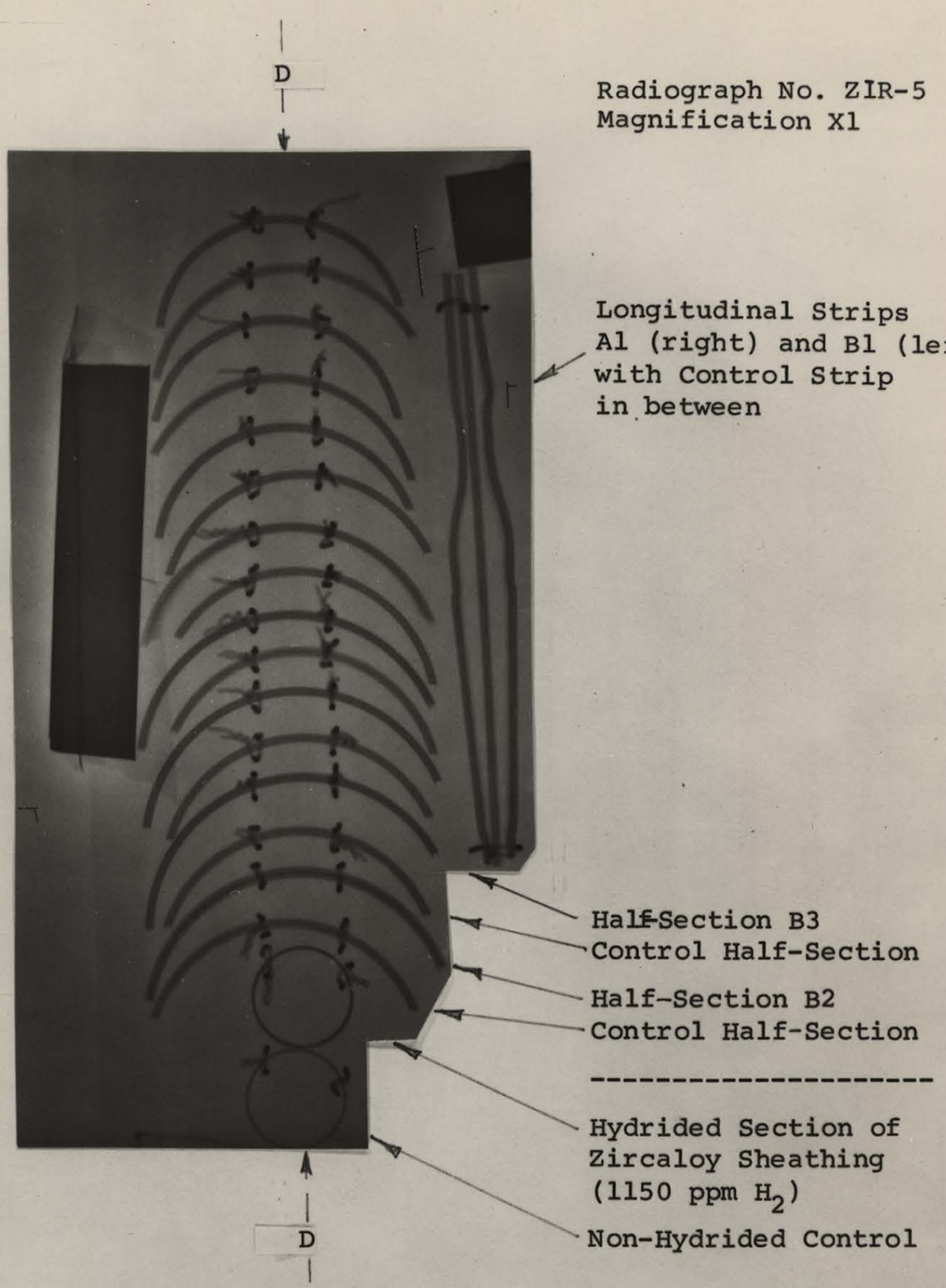

Figure 9 Positive print from the neutron radiograph of the B-series of half-sections and longitudinal strips A1 and B1

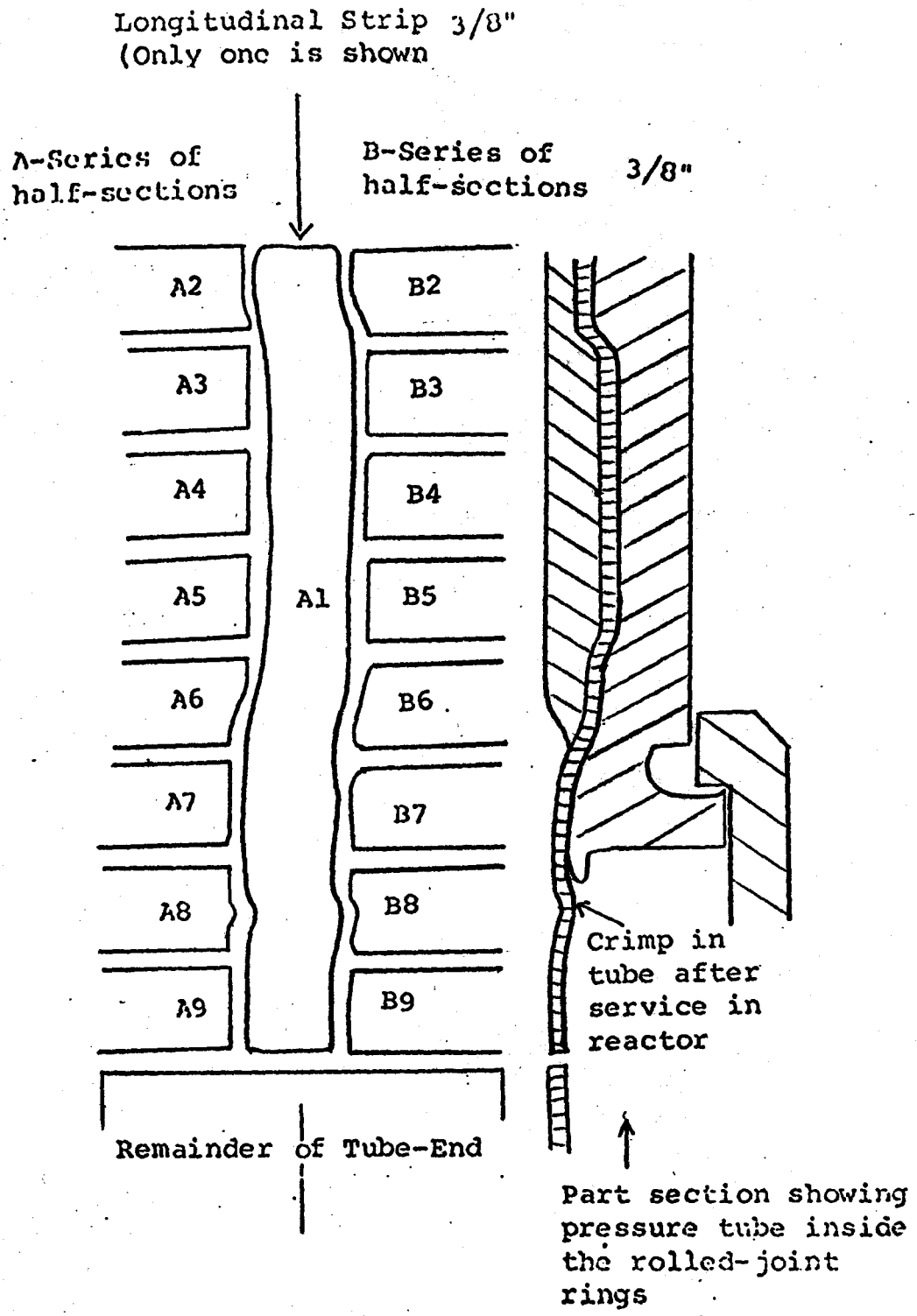

Figure 7 Cutting scheme for top end of X-7 Mark VI Pressure Tube

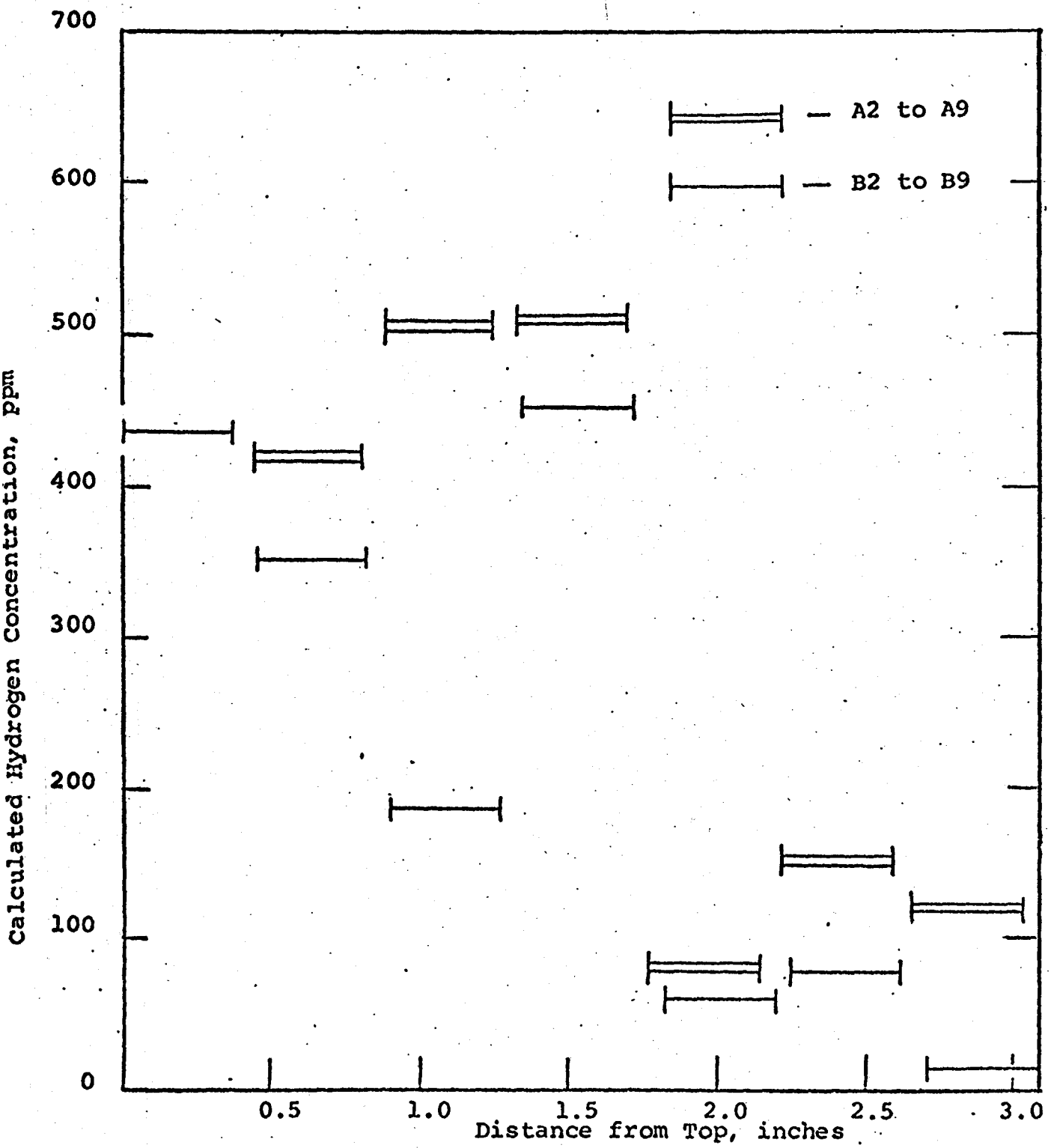

Figure 10 Hydrogen concentrations in the A- and B-series of half-sections

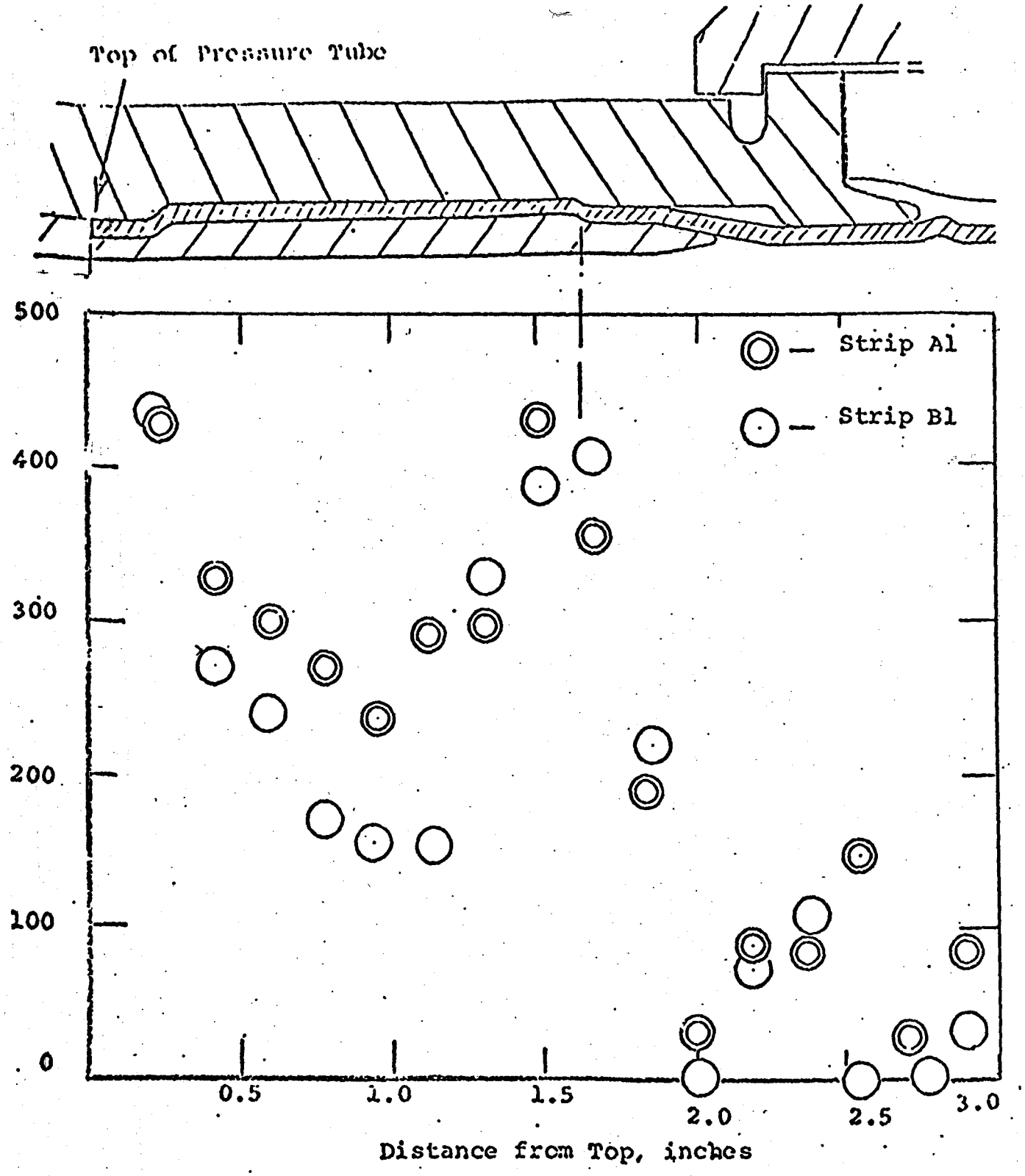

Figure 11 Hydrogen distribution along longitudinal strips A1 and B1 from the X-7 Mark VI pressure tube

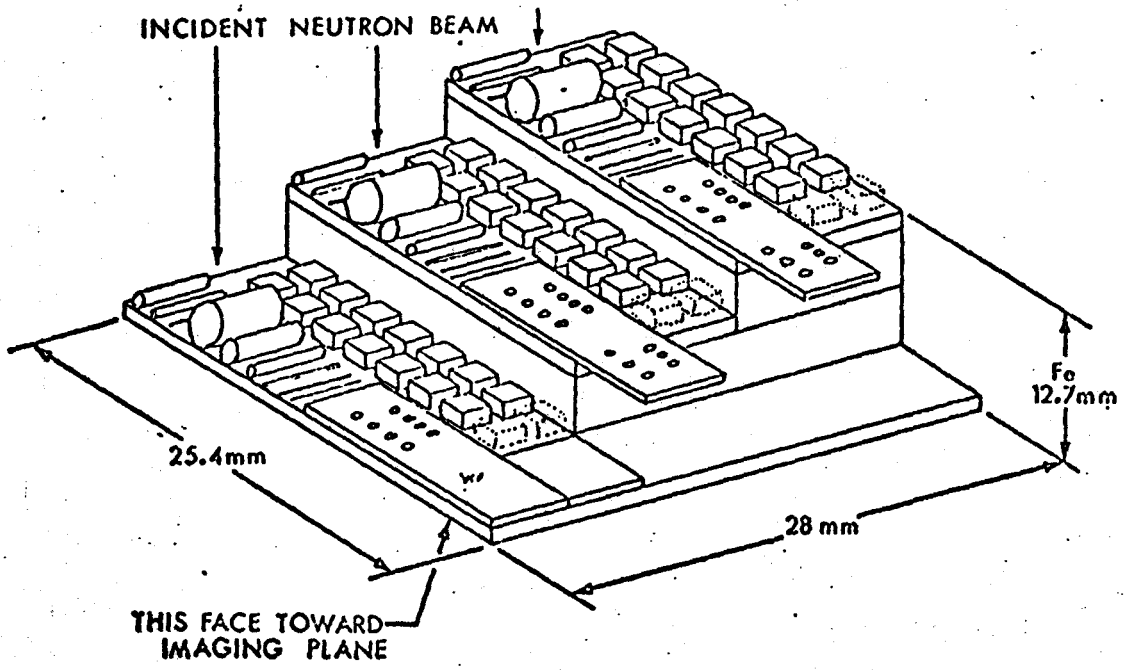

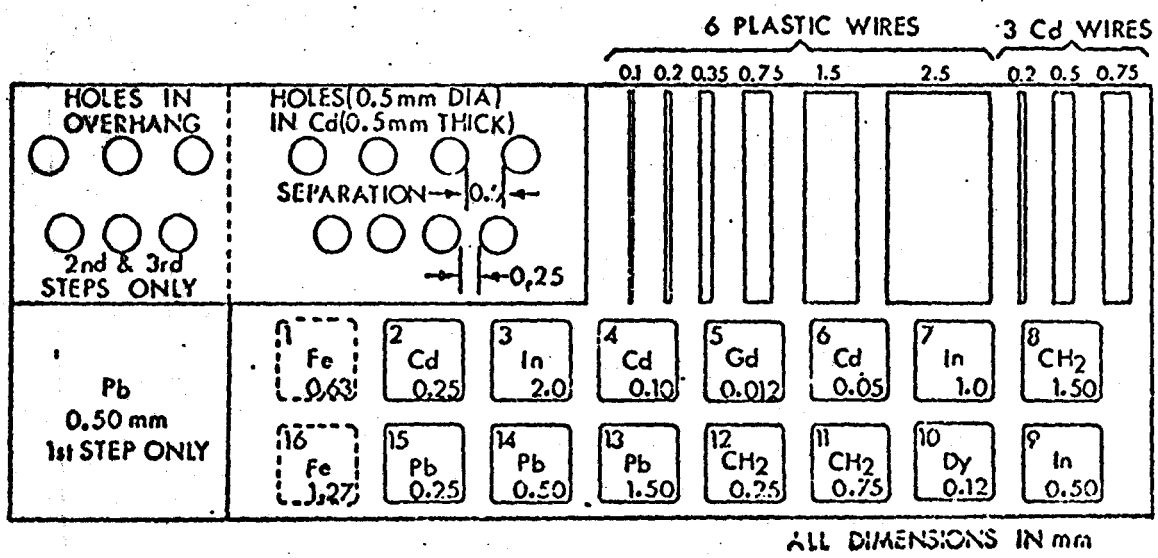

Figure 12 Sketches showing the construction of the [illegible] test object

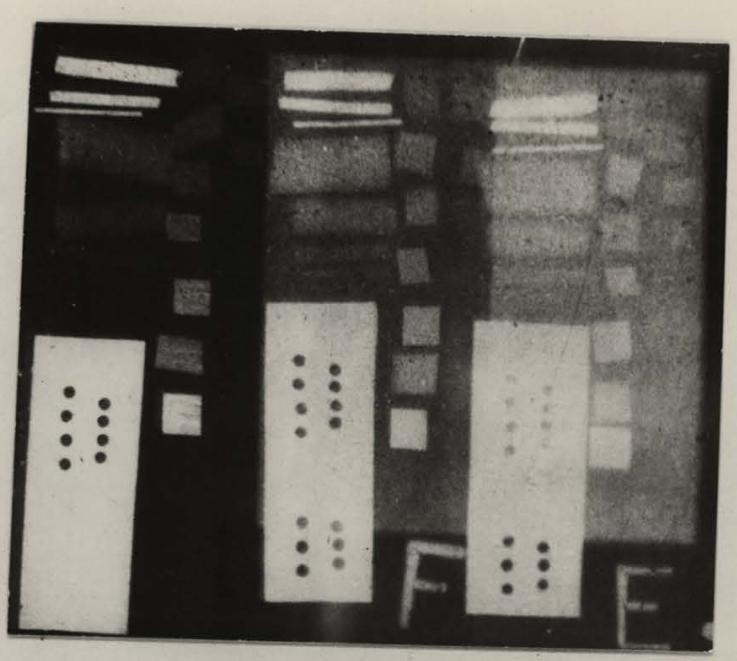

(a)

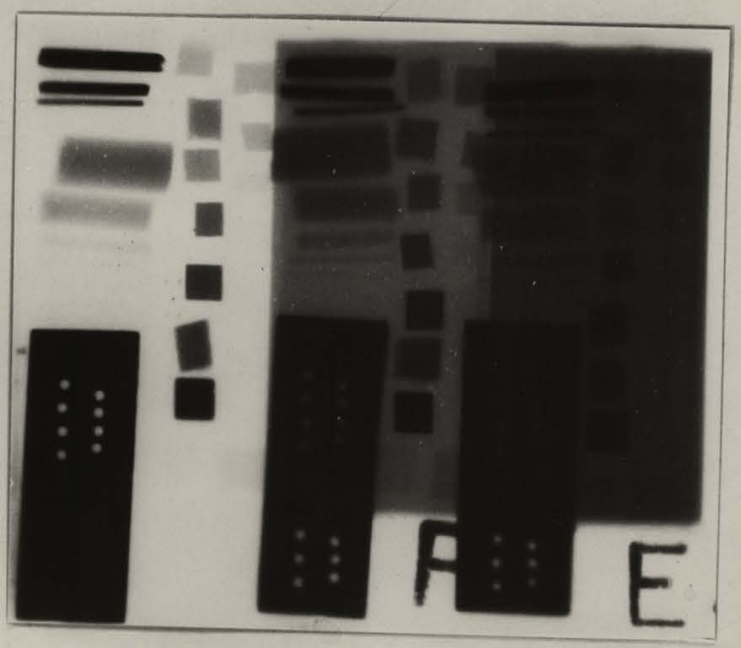

(b)

Figure 13 Thermal neutron radiographs of a VISQUI test object; (a) Track-etch technique; (b) transfer-exposure method
Magnification 3X

(a)

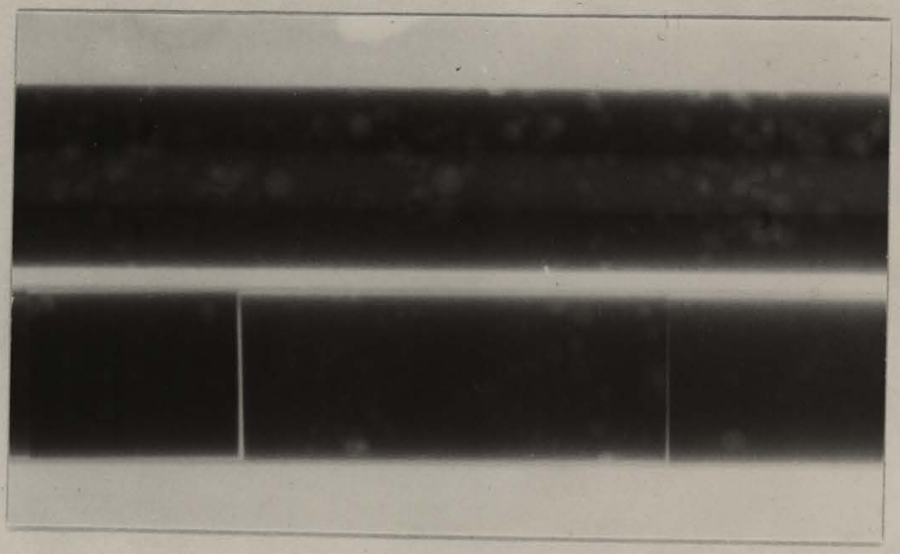

(b)

Figure 14 Thermal neutron radiographs of long hollow (upper) and short slugs of cast metal fuel (a) Track-etch technique; (b) transfer-exposure method

Magnification 2x (a)
1.5x(b)

MICROWAVE MEASUREMENTS OF INSULATOR MATERIALS

by

P.S.W. Chan

PART B: MCMASTER (ON-CAMPUS) PROJECT*

A project report submitted in partial fulfilment of the requirements for the degree of Master of Engineering

Department of Engineering Physics
McMaster University

April 1974

*One of two project reports: The other part is designated
PART A: INDUSTRIAL PROJECT REPORT

TITLE (PART B.) : Microwave Measurements Of Insulator Materials

AUTHOR : P.S. W. Chan

SUPERVISOR : Dr. C. K. Campbell

NUMBER OF PAGES: ii, 26

MASTER OF ENGINEERING
(ENGINEERING PHYSICS)

McMASTER UNIVERSITY
Hamilton, Ontario

INDEX

ACKNOWLEDGEMENT

I wish to thank Dr. C. K. Campbell for his supervision of this project.

ABSTRACT

A method for measuring the complex permittivity of insulator materials at microwave frequencies is described in detail. Results of dielectric measurements using this technique are in good agreement with data from other sources. MKS units are used in this report.

1. Introduction

One of the factors which indicates the quality of an insulator material is its complex permittivity (dielectric constant) , the imaginary part of which gives the loss factor of the insulator. At low to medium frequencies, e.g. up to 10^8 hertz, conventional impedance bridge methods can be used to measure the complex permittivity of a dielectric material. Since most insulators have very low losses, at high frequencies, i.e. 10^9 Hz and above, radiation loss and skin effect of lumped circuit elements seriously affect the accuracy of impedance bridge measurements, resonant cavity methods are often used for dielectric measurements at microwave frequencies. The following sections describe a technique suitable for measuring the complex permittivity of insulator slabs using a rectangular resonant cavity at frequencies above 10^9 hertz.

2. Concept Of Complex Permittivity

Consider an evacuated parallel plate condenser connected to a sinusoidal voltage $V_o \sin wt$ as shown in Figure (1a), the condenser stores a charge Q and draws a charging current I_c , where Q and I_c are related by the following equations,

$$V = V_o \, e^{jwt} \qquad \ldots\ldots\ldots\ldots \quad 2.1$$

$$w = 2\pi f \qquad \ldots\ldots\ldots\ldots\ldots \quad 2.2$$

$$Q = C_o V \qquad \ldots\ldots\ldots\ldots\ldots \quad 2.3$$

$$I_c = \frac{dQ}{dt}$$

$$= jwC_oV$$

$$= I_o e^{j(wt + \frac{\pi}{2})} \qquad \ldots\ldots\ldots\ldots 2.4$$

where f = frequency of the sinusoidal voltage in hertz

Q = charge stored in the condenser

C_o = Capacitance of the condenser when vacuum is its dielectric

I_c = Charging current

when the condenser is filled with other dielectric, its capacitance is increased to

$$C = C\frac{\epsilon'}{o\epsilon_o} = C_o\ e'_r \qquad \ldots\ldots\ldots\ldots 2.5$$

where

e_o = real permittivity of vacuum, 8.85×10^{-12} farad/meter

e' = real permittivity of the dielectric

e'_r = relative real permittivity of the dielectric

Since most dielectric materials are not perfectly lossless, therefore in addition to the charging current I_c , a loss current I_l also appears across the terminals of the condenser, and

$$I_l = GV \qquad \ldots\ldots\ldots\ldots 2.6$$

where G = conductance of the condenser in mho

Figure (1b) shows that I_c leads the applied voltage V by a phase angle of 90°, I_l in phase with the voltage and the resultant current I is inclined by a power factor angle θ against the voltage and by a loss angle δ against the + j axis, where

$$I = I_c + I_l = (jwC + G) V \qquad \ldots\ldots 2.7$$

$$\theta = \tan^{-1} \frac{I_c}{I_l} \qquad \ldots\ldots 2.8$$

$$\delta = 90^\circ - \theta \qquad \ldots\ldots 2.9$$

The loss in dielectric materials does not necessarily originate entirely from the finite conductance of electrical charges across the material, but may also represent any other energy consuming process, therefore it is customary to refer to the existance of a loss current in addition to the charging current by the introduction of a complex permittivity

$$\epsilon^* = \epsilon' + j\epsilon'' \qquad \ldots\ldots 2.10$$

and equation 2. 7 may be rewritten as

$$I = (jw\epsilon' - w\epsilon'') \frac{C_o}{e_o} V$$

$$= jwC_o \epsilon_r^* V \qquad \ldots\ldots 2.11$$

$$\text{and} \quad \epsilon_r^* = \frac{\epsilon^*}{\epsilon_o} = \epsilon_r' + j\epsilon_r'' \qquad \ldots\ldots\ldots \quad 2.12$$

where ϵ_r^* is the complex relative permittivity of the dielectric material and ϵ'' and ϵ_r'' are the loss factor and relative loss factor respectively. The dissipation factor D, or loss tangent, $\tan \delta$, may be defined as

$$D = \tan \delta = \frac{\epsilon''}{\epsilon'} = \frac{\epsilon_r''}{\epsilon_r'} \qquad \ldots\ldots\ldots \quad 2.13$$

3. Perturbation Effect Of A small Foreign Dielectric Object In A Resonant Cavity

Consider an empty cavity which is resonating at a frequency f_o, when a small dielectric object is inserted into this cavity the resonant frequency of the resultant cavity is reduced to a lower value f_s. The reduction in resonant frequency is given by (Ref. 4)

$$\frac{\delta f_s}{f_s} = \frac{-\int_{V_s} (\mu_s H_s^2 - \epsilon_s E_s^2) \, dv}{\int_V (\mu_o H_o^2 - \epsilon_o E_c^2) \, dv} \qquad \ldots\ldots\ldots \quad 3.0.1$$

where

$$\delta f_s = f_o - f_s$$

μ_o , μ_s = real permeability of air and dielectric object respectively

V , V_s = Volume of the cavity and object respectively

ϵ_o, ϵ_s = real permittivity of air and object respectively

H_o, H_s = magnetic field in air and object respectively

E_o, E_s = electric field in air and object respectively

The total energy stored in the cavity, U may be calculated from

$$U = \frac{\int_V (\mu_o H_c^2 - \epsilon_o E_c^2)\, dv}{4} \qquad \ldots\ldots\ldots \quad 3.0.2$$

Hence equation 3.0.1 may be rewritten as

$$\frac{\delta f_s}{f_s} = \frac{-\int_{V_s} (\mu_s H_s^2 - \epsilon_s E_s^2)\, dv}{4U} \qquad \ldots\ldots\ldots \quad 3.0.3$$

Equation 3.0.3 relates the perturbation in cavity resonant frequency due to the foreign dielectric object. Imagine that we have another dielectric object of identical geometry but slightly different dielectric constant , i.e.

$$\epsilon_1 = \epsilon_s + \delta\epsilon_1$$

$$\mu_1 = \mu_s$$

when this object is inserted into the cavity, a further reduction in resonant frequency to f_1 will be observed. Assuming that the electric and magnetic field inside the objects are the same as before, we may write

$$\frac{\delta f_1}{f_1} = \frac{-\int_{V_s} (\mu_s H_s^2 - e_1 E_s^2) \, dv}{4 U} \qquad \ldots\ldots\ldots \quad 3.0.4$$

$$\delta f_1 = f_o - f_1 \qquad \ldots\ldots\ldots \quad 3.0.5$$

in the limit $e_1 \longrightarrow e_s + de_1$ 3.0.6

$\delta f_1 - \delta f_s \longrightarrow - df_1$ 3.0.7

$f_s \longrightarrow f_1$ 3.0.8

we can combine equations 3.0.3 and 3.0.4 to get

$$\frac{- df_1}{f_1} = \frac{de_1 \int_{V_s} E_s^2 \, dv}{4 U}$$

or

$$\int_{V_s} E_s^2 \, dv = - \frac{4U \, df_1}{f_1 \, de_1} \qquad \ldots\ldots\ldots \quad 3.0.9$$

Equation 3.0.9 relates the integral of electric field in the dielectric object to the derivative $\frac{1}{f_1} \frac{df_1}{de_1}$, which can be derived experimentally or theorectically for certain cavity and object geometries. Various methods are available (Ref. 5) for measuring the real part of the complex permittivity using

resonant cavity method. It is especially useful for measuring the loss factor of a dielectric material in resonant cavity methods where the integral of electric field in the object is often encountered.

3.1 Relation Of The Loss Tangent Of A Dielectric Object And Resonant Cavity Q Factors

The Q factor of an empty resonant cavity may be defined as

$$Q_o = \frac{2\pi \times \text{total energy stored in cavity}}{\text{energy dissipated per period}}$$

$$= \frac{2\pi U}{L_o} \qquad \ldots\ldots\ldots\ldots \quad 3.1.1$$

where L_o = energy dissipated per period of the empty cavity

If a dielectric object is inserted into the cavity, the Q factor of the cavity will be reduced to

$$Q_1 = \frac{2\pi U}{L_o + L_d} \qquad \ldots\ldots\ldots \quad 3.1.2$$

where L_d = loss in the dielectric object

hence $$\frac{1}{Q_1} - \frac{1}{Q_o} = \frac{L_d}{2\pi U} \qquad \ldots\ldots\ldots 3.1.3$$

evaluated either analytically or numerically using a digital computer once an expression relating f_1 and ϵ_1 has been found.

4. Measurement Of Complex Permittivity Of A Dielectric Slab Using A Rectangular Resonant Cavity

4.1 Dielectric Slab At The End Of Cavity

Figure (2a) illustrates the case where a slab of dielectric material of thickness l_1 is placed at the end of a rectangular resonant cavity. The dimensions of the cavity are such that only TE_{101} mode wave can propagate in the Z direction of the cavity. The resonant frequency of the empty cavity is given by

$$f_o = \frac{C}{2}\sqrt{\frac{1}{a^2} + \frac{1}{d^2}} \qquad \ldots\ldots\ldots \quad 4.1.1$$

where C = velocity of light in free space

a, d = length and depth of the rectangular cavity

The cut-off wavelength is given by

$$\lambda c = 2a \qquad \ldots\ldots\ldots \quad 4.1.2$$

at $Z = l_o$, looking towards the right, we have, from transmission line theory

$$Z(l_o) = Z_1 \tanh \gamma_1 l_1 \qquad \ldots\ldots\ldots \quad 4.1.3$$

and looking towards the left, we have

$$Z(l_o) = -Z_o \tanh \gamma_o l_o \qquad \ldots\ldots\ldots \quad 4.1.4$$

where Z_1, γ_1, Z_o, γ_o are the intrinsic impedance and propagation factor in the dielectric and air filled region respectively.

Equating equations 4.1.3 and equation 4.1.4 , we get

$$Z_1 \tanh \gamma_1 l_1 = -Z_o \tanh \gamma_o l_o \qquad \ldots\ldots\ldots \quad 4.1.5$$

For frequencies above cut-off, γ_1 and γ_o are purely imaginary numbers, and (Ref. 5)

$$\gamma_1 = \frac{j2\pi}{c}\sqrt{f_1^2 \frac{\epsilon_1}{\epsilon_o} - \left(\frac{c}{\lambda_c}\right)^2} \qquad \ldots\ldots\ldots \quad 4.1.6$$

$$= j\beta_1$$

$$\gamma_o = \frac{j2\pi}{c}\sqrt{f_o^2 - \left(\frac{c}{\lambda_c}\right)^2} \qquad \ldots\ldots\ldots \quad 4.1.7$$

$$= j\beta_o$$

where β_1 and β_o are the phase constants of the dielectric and air filled regions , and f_1, f_o are the resonant frequencies of the cavity with and without the dielectric slab respectively .

Equation 4.15 can be rewritten as

$$Z_1 \tan \beta_1 l_1 = -Z_o \tan \beta_o l_o \quad \ldots\ldots\ldots 4.1.8$$

and since from transmission line theory,

$$\frac{Z_1}{Z_o} = \frac{\gamma_o}{\gamma_1} = \frac{\beta_o}{\beta_1} \quad \ldots\ldots\ldots 4.1.9$$

Substituting equation 4.1.9 into equation 4.1.8, we obtain

$$\frac{\tan \beta_1 l_1}{\beta_1} = - \frac{\tan \beta_o l_o}{\beta_o}$$

$$\text{i.e.} \quad \frac{\tan \beta_1 l_1}{\beta_1 l_1} = - \frac{\tan \beta_o l_o}{\beta_o l_1} \quad \ldots\ldots\ldots 4.1.10$$

Rearranging equation 4.1.6, we have

$$\epsilon_1 = \epsilon_o \left(\frac{c}{f_1}\right)^2 \left[\left(\frac{1}{\lambda c}\right)^2 + \left(\frac{\beta_1 l_1}{2 \pi l_1}\right)^2 \right] \quad \ldots\ldots\ldots 4.1.11$$

Equation 4.1.11 is the relationship between the real part of the complex permittivity of the dielectric material, i.e. ϵ_1, and the resonant frequency of the cavity with the dielectric slab at the end. The quantity $\beta_1 l_1$ is obtained from the solution of

of equation 4.1.10, which is a transcendental equation of the form $\frac{\tan A}{A} = B$, In general, the solution of $\beta_1 l_1$ from equation 4.1.10 is not unique, however, since only TE_{101} mode wave can propagate in the cavity, the desired solution is the first positive value of $\beta_1 l_1$ that satisfies equation 4.1.10. Although it is not possible to evaluate $\frac{df_1}{d\epsilon_1}$ analytically from equation 4.1.11 , the derivative can be readily computed by standard numerical differentiation technique using a digital computer. Referring back to equation 3.1.7 , we see that Q_1 , Q_o can be obtained by measuring the bandwidths of the resonant curves of the cavity with and without the slab, ϵ_1 and the derivative $\frac{df_1}{d\epsilon_1}$ can be computed from equation 4.1.11, therefore the loss tangent , $\tan \delta$, can be evaluated. This means that both the real and imaginary part of the complex permittivity of the dielectric material can be determined by measuring the resonant frequencies and bandwidths of the cavity before and after insertion of the slab.

4.2 Dielectric Slab At The Center Of Cavity

Consider the case when a dielectric slab is placed at the center of a rectangular cavity as shown in Figure (2b). The analysis leading to the determination of the complex permittivity of the

dielectric material is essentially identical to that of the previous case. By summing the impedances seen at $Z=l_o$, we get

$$Z_1 \cot \beta_1 l_1 = Z_o \tan \beta_o l_o \qquad \ldots\ldots\ldots \quad 4.2.1$$

Using equation 4.1.9 , we arrive at

$$\frac{\cot \beta_1 l_1}{\beta_1 l_1} = \frac{\tan \beta_o l_o}{\beta_o l_1} \qquad \ldots\ldots\ldots \quad 4.2.2$$

And finally by rearranging equation 4.1.6 we have

$$e_1 = e_o \left(\frac{c}{f_1}\right)^2 \left[\left(\frac{1}{\lambda c}\right)^2 + \left(\frac{\beta_1 l_1}{2\pi l_1}\right)^2\right] \qquad \ldots\ldots\ldots \quad 4.2.3$$

Equation 4.2.3. is identical to 4.1.11, however, the quantity $\beta_1 l_1$ is now obtained from the solution of equation 4.2.2, which is in the form $\frac{\cot A}{A} = B$, the discussions in the previous section are still valid here, therefore the desired solution of equation 4.2.2 is the first positive value of $\beta_1 l_1$ that satisfies the equation. Once again the loss tangent of the dielectric can be computed from equation 3.1.7 .

5. Experimental Measurements Of Complex Permittivity Of Various Dielectric Materials

5.1 Experimental Procedures

The set up of the equipments required for the measurement of complex permittivity of a slab of dielectric materials is illustrated in Figure (3) . The X-13 variable frequency klystron used in this work is a two-watt maximum power output klystron which can be mechanically tuned over the frequency range from eight to twelve gigerhertz. A single-stub tuner is used to match the resonant cavity to the waveguide transmission system so that zero power is reflected from the cavity when the klystron is operating at the cavity resonant frequency. The frequency response,i.e. resonant curve of the cavity is displayed on a 10 MHz dual beam oscilloscope connected to test points 1 and 2. Test point 1 monitors the input power to the cavity whereas test point 2 monitors the reflected power from the cavity. The resonant frequency of the cavity at a particular setting can be determined by adjusting the wavemeter until a dip occurs at the zero power point on the cavity resonant curve on the oscilloscope with input signal from test point 2.

Slabs of dielectric materials, e.g. lucite, polystyrene and alumina substrate (often used for microwave thin film circuit components) are machined to the exact cross-sectional dimensions of the cavity. The resonant frequency and bandwidth of the empty cavity are measured as mentioned above. The dielectric slab is then fitted snugly into the cavity and placed either

in the middle or at the end of the cavity, depending on whether the analysis of section 4.1 or 4.2 is used for the complex permittivity measurements. The resonant frequency and bandwidth of the loaded cavity are again measured. The two sets of resonant frequencies and bandwidths, together with the dimensions of the cavity and slab uniquely define the complex permittivity of the material in the slab.

5.2 Calculation Of Complex Permittivity From Resonant Cavity Measurement

A FORTRAN program DIEL has been written to calculate the complex permittivity of the material in the dielectric slab using the resonant cavity measurement data obtained from section 5.1 . The program requires one input data card containing the following variables in the Format (7F10.0, I10), one blank card after the data terminates the program,

A = width of the cavity in meter (x - axis)

B = height of the cavity in meter (y - axis)

F(1) = resonant frequency of empty cavity, in GHz

F(2) = resonant frequency of cavity containing the slab in GHz

Q1 = bandwidth of empty cavity, in GHz

Q2 = bandwidth of cavity with dielectric slab, in GHz

XLE = thickness of the slab in meter

MP = 0 if slab is at the end of cavity

= 1 if slab is at the center of cavity

The program evaluates the desired solution of $\beta_1 l_1$ in the transcendental equation 4.1.10 or 4.2.2 depending on the position of the slab in the cavity, ϵ_1, the real part of the complex permittivity is then calculated from equations 4.1.11 or 4.2.3 . The derivative $\frac{df_1}{de_1}$ is then calculated by numerical differentiation using equation 4.1.11 or 4.2.3 and finally, $\tan\delta$, the loss tangent or dissipation factor of the dielectric material is computed from equation 3.1.7 .

5.3 Comments On The Results Of Resonant Cavity Measurements

The results of the complex permittivity measurements of slabs of lucite, polystyrene and alumina substrate are tabulated in Table (1) . In general, for the same material, ϵ_1 varies within $\pm 5\%$ and $\tan\delta$ varies within $\pm 15\%$. The values $\frac{\epsilon_1}{\epsilon_0}$ $\tan\delta$, listed in Table (1) are therefore the mean values chosen from a representative set of measurements. The major sources of errors in the measurements are most likely due to the imperfectness of sample preparation and the low resolution of the wavemeter-oscilloscope system for resonant frequency and

and bandwidth measurements. Complex permittivity data for the same materials from other sources are also listed in Table (1), it is evident that the results from resonant cavity measurements are comparable to those from other methods.

5.4 Conclusion

A microwave measurement technique using a resonant cavity has been developed and successfully applied to the measurement of the complex permittivity of various insulator materials at frequencies above nine gigerhertz. Although equations are specifically derived for insulator slabs in rectangular resonant cavities, this technique can be extended to treat other insulator and cavity geometries provided that theoretical relationship between the real part of the complex permittivity of the insulator material and the loaded cavity resonant frequency can be established.

References

1. Werner Rueggeberg, " Determination of Complex Permittivity of Arbitrarily Dimensioned Dielectric Modules at Microwave Frequencies " , IEEE Transaction on Microwave Theory And Techniques, Vol. MTT-19, No.6, June 1971

2. A. Von Hippel, " Dielectric Materials and Application ", Cambridge, Mass, MIT Press,1954.

3. Walter H. Gitzen, " Alumina As A Ceramic Material ", The American Ceramic Society, Inc.,1970

4. Emile Argence and Théo Kahan, " Theory of Waveguides and Cavity Resonators ", Blackie and Son Ltd., 1966

5. Max Sucher and Jerome Fox, " Handbook of Microwave Measurements ", Wiley, 1963, Volume 2, 3rd. Edition

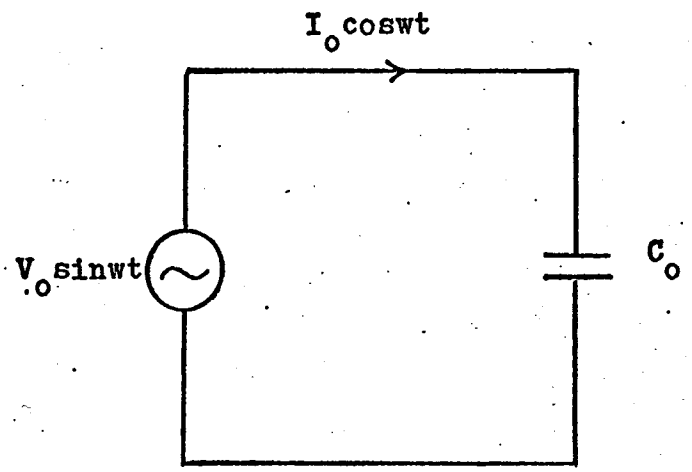

Figure 1a Capacitor Connected Across Sinusoidal Voltage Source

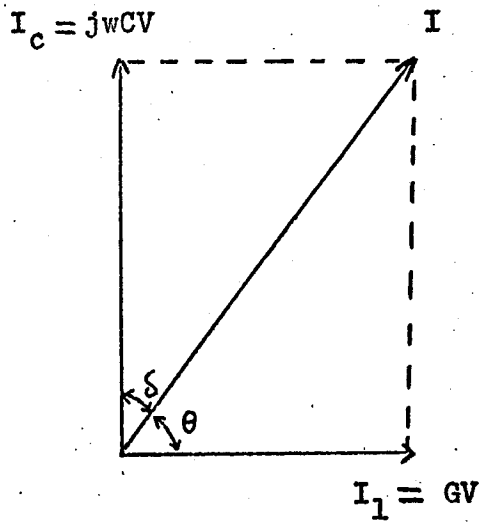

Figure 1b Loss Current I_1 And Charging Current I_c In Capacitor Containing Dielectric Material With Loss

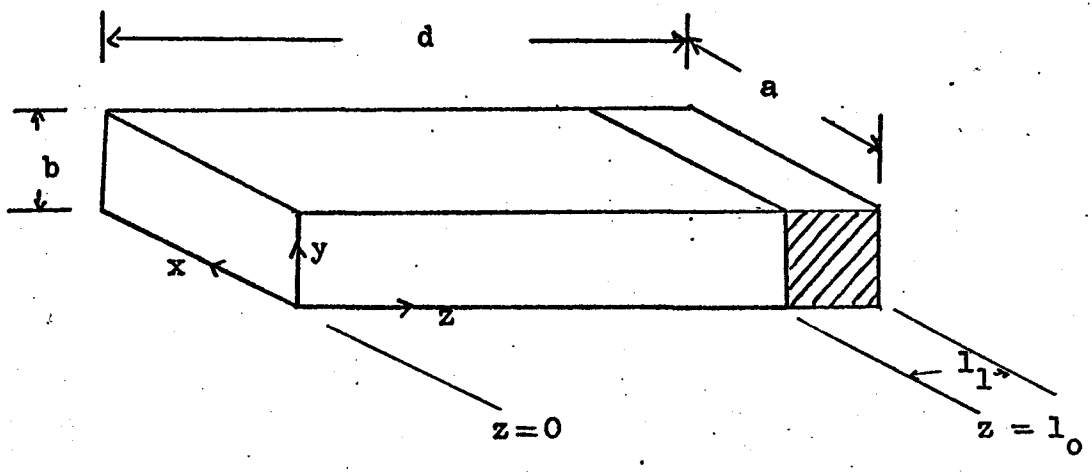

Figure 2a Dielectric Slab At The End Of Cavity

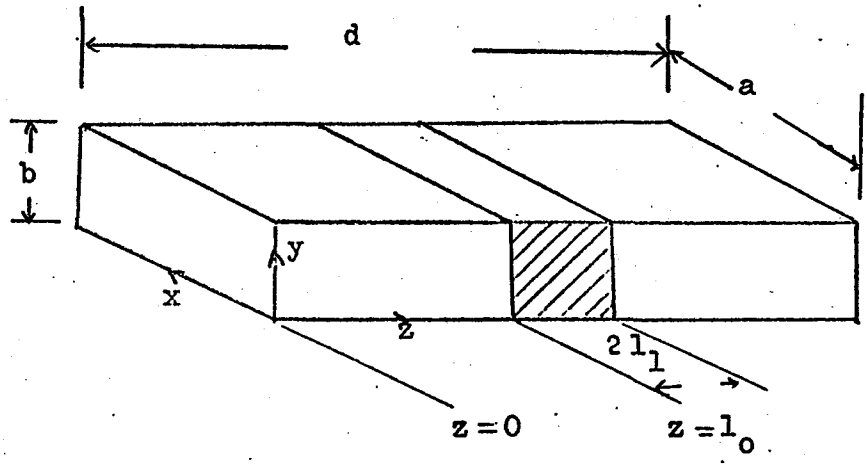

Figure 2b Dielectric Slab At Cavity Center

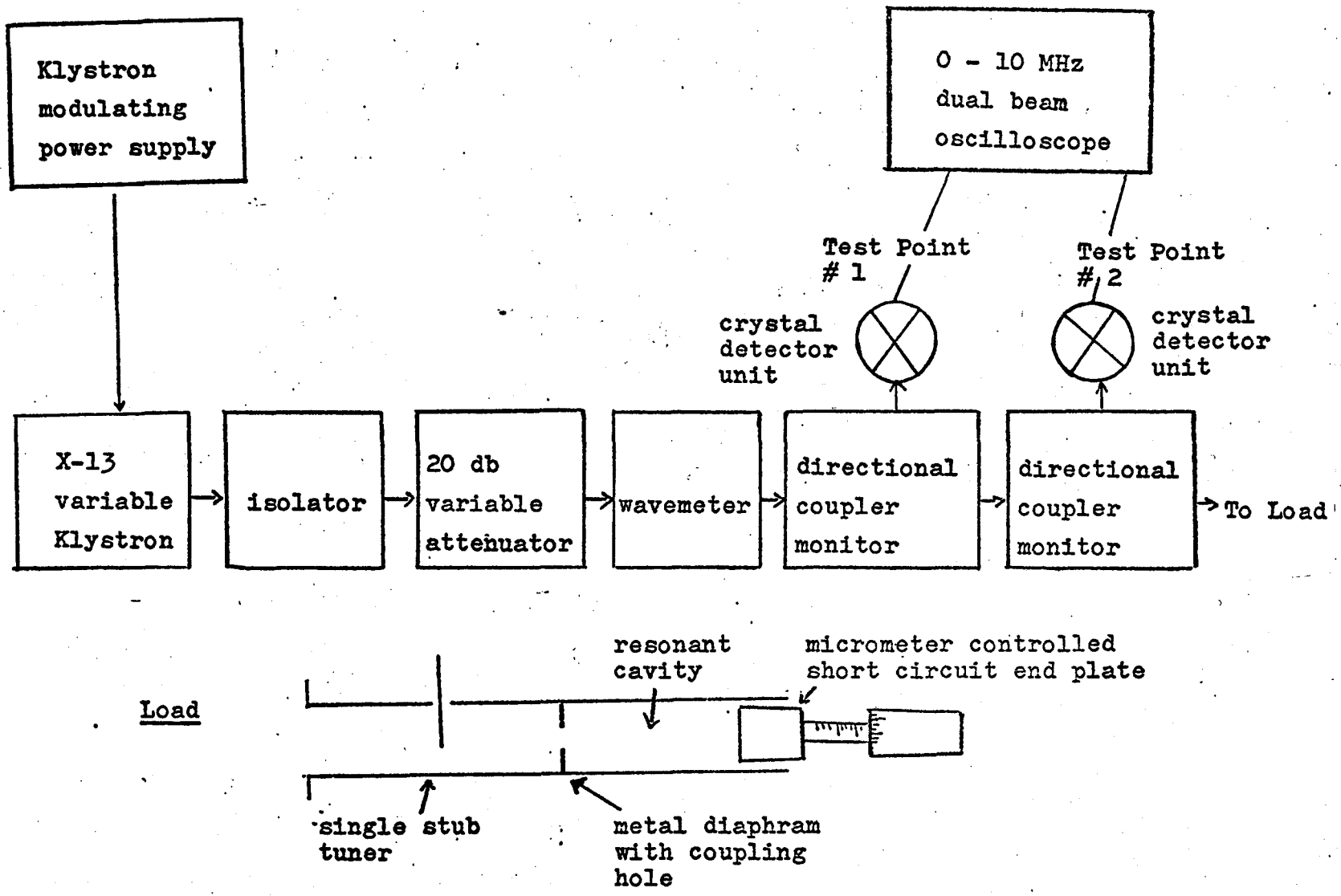

Figure (3) Resonant Cavity Measurement System

Dielectric material	Position in resonant Cavity	Thickness of slab	Frequency	Resonant Cavity measurement		other methods	
		cm.	10^9 hertz	e_1/ϵ_o	tan δ	e_1/ϵ_o	tan δ
Lucite	End	0.317	9.331	2.64	0.0075	2.63[a]	0.0055[a]
	End	0.156	9.358	2.61	0.0081	to	to
	Middle	0.156	9.274	2.58	0.0078	2.65	0.0080
Polystyrene	End	0.318	9.397	2.56	0.00085	2.53[b]	0.00043[b]
	End	0.158	9.371	2.55	0.00081	to	to
	Middle	0.158	9.368	2.54	0.00079	2.55	0.00069
Alumina Substrate	End	0.137	9.366	9.27	0.00015	9.0 [c]	0.00010[c]
	End	0.0685	9.375	9.32	0.00014	to	to
	Middle	0.0685	9.321	9.38	0.00013	10.0	0.00020

a Data from ref.(1)
b Data from ref.(2)
c Data from ref.(3)

Table (1) Complex Permittivity Of Several Insulator Materials

```
      PROGRAM DIEL(INPUT,OUTPUT,TAPE5=INPUT,TAPE6=OUTPUT)
      DIMENSION F(10),Q(10),FF(3)
C     THIS PROGRAM CALCULATES THE RELATIVE COMPLEX PERMITTIVITY
C     OF A DIELECTRIC SLAB USING CAVITY RESONANT MEASUREMENT DATA
1     READ (5,10) A,B,F(1),F(2),Q1,Q2,XLE,MP
C     A,B ARE DIMENSIONS OF THE RESONANT CAVITY IN METER
C     C IS THE VELOCITY OF LIGHT IN METERS' PER SECOND
C     TC IS THE CUT OFF WAVELENGTH OF THE CAVITY IN METER
C     MP=0 IF SAMPLE IS AT END OF CAVITY,1 IF IN CENTER
C     F(1),F(2) ARE THE EMPTY AND LOADED CAVITY RESONANT
     *FREQUENCY IN GIGERHERTZ
C     Q1,Q2 ARE THE BANDWIDTH OF THE EMPTY AND LOADED CAVITY
     *IN GIGERHERTZ
C     XLE IS THE THICKNESS OF DIELECTRIC SAMPLE IN METER
      IF(XLE.LE.0.0) STOP
C     ONE BLANK CARD TERMINATES THE PROGRAM
      C=3.0*10.0**8.0
      TC=2.0*A
      XY=1.0*10.0**9.0
      F(1)=F(1)*XY
      F(2)=F(2)*XY
      Q1=Q1*XY
      Q2=Q2*XY
      Q(1)=F(1)/Q1
      Q(2)=F(2)/Q2
      DE=XLE
      FRO=F(1)
      WRITE(6,20)
      WRITE(6,25) A,B,D,XLE,FRO
      IF(MP.EQ.0) D=D/2.0
      XLO=D-XLE
      FF(1)=F(2)
      FF(2)=FF(1)-5.0-10.0**4.0
      FF(3)=FF(1)-5.0*10.0**4.0
```

```
      DO 500 N=1,3
      FR=FF(N)
      CALL SUB1(FR,TC,XKR)
      XKR1=XKR
      X1=XKR1*XLO
      X2=XKR1*XLE
      XK=(TAN(X1))/X2
      IF(MP.EQ.0) CALL SUB2(XK,X,NN)
      IF(MP.EQ.1) CALL SUB6(XK,X,NN)
      Z=X
      M=NN
      CALL SUB3(Z,XLE,TC,FR,E)
      EE(N)=E
500   CONTINUE
      CALL SUB5(EE,FF,Q(1),Q(2),S)
      E=EE(1)
      RATIO=FRO/F(2)
      WRITE (6,100) M,E,S,F(2)
      GO TO 1
10    FORMAT(7F10.0,I10)
20    FORMAT(1H1)
25    FORMAT(10X,* CAVITY LENGTH *,F10.6,10X,* CAVITY WIDTH *,
     -F10.6,10X,* CAVITY DEPTH *,F10.6//10X,* SAMPLE THICKNESS *,
     -F10.6,10X,* EMPTY CAVITY RESONANT FREQUENCY *,E12.6//)
100   FORMAT(10X,* NO. OF ITERATION *,I5,10X,* DIELECTRIC CONSTANT*,
     -F6.3/10X,* DISSIPATION FACTOR *,F10.5,* LOADED CAVITY *,
     -*RESONANT FREQUENCY *,E12.6//)
      STOP
      END
```

```
      SUBROUTINE SUB1(FRI,TC,XKR)
      C=3.0*10.0**8.0
      A=2.0*3.14159/C
      B=ABS((FRI*FRI)-(C/TC)**2.0)
      B=B**0.5
      XKR=A*B
      RETURN
      END
      SUBROUTINE SUB2(XK,X,M)
      A=0.0001
      B=1.570
      DO 500 N=1,50
      C=(A+B)/2.0
      FA=A*XK-COTAN(A)
      FB=B*XK-COTAN(B)
      FC=C*XK-COTAN(C)
      IF(FB*FC.GT.0.0) B=C
      IF(FA*FC.GT.0.0) A=C
      M=N
      X=C
      TXK=COTAN(X)/X
      EF=(ABS(TXK)-ABS(XK))/XK
      AF=0.00001
      IF(ABS(EF).LE.AF) GO TO 600
500   CONTINUE
600   X=C
      RETURN
      END
      SUBROUTINE SUB3(X,XLE,TC,FR,E)
      C=3.0*10.0**8.0
      A=(1.0/TC)**2.0
      B=(X/(2.0*3.14159*XLE))**2.0
      E=(C/FR)**2.0*(A B)

      RETURN
      END
```

```
      SUBROUTINE SUB4(Y,YK,FY)
      FY=Y*YK+TAN(Y)
      RETURN
      END
      SUBROUTINE SUB5(EE,FF,Q1,Q2,S)
      DIMENSION EE(3),FF(3),AA(3)
      A=(1.0/Q2-1.0/Q1)
      B=FF(1)/EE(1)
      IF(EE(2).EQ.EE(3)) GO TO 100
      C=(FF(2)-FF(3))/(EE(2)-EE(3))
      S=(-1.0)*A*B/(2.0*C)
      RETURN
100   S=0.0
      RETURN
      END
      SUBROUTINE SUB6(XK,X,M)
      A=0.0001
      B=1.570
      DO 500 N=1,50
      C=(A+B)2.0
      C=(A+B)/2.0
      FA=A*XK+TAN(A)
      FB=B*XK+TAN(B)
      FC=C*XK+TAN(C)
      IF(FB*FC.GT.0.0) B=C
      IF(FA*FC.GT.0.0) A=C
      M=N
      X=C
      TXK=TAN(X)/X
      EF=(ABS(TXK)-ABS(XK))/XK
      AF=0.00001
      IF(ABS(EF).LE.AF) GO TO 600
500   CONTINUE
600   X=C
      RETURN
      END
```